Atmospheric
Chemistry
and Physics

Quasi-12 h inertia–gravity waves in the lower mesosphere observed by the PANSY radar at Syowa Station (39.6° E, 69.0° S)

Ryosuke Shibuya[1], **Kaoru Sato**[1], **Masaki Tsutsumi**[2,3], **Toru Sato**[4], **Yoshihiro Tomikawa**[2,3], **Koji Nishimura**[2,3], and **Masashi Kohma**[1]

[1]Department of Earth and Planetary Science, The University of Tokyo, Tokyo, Japan
[2]National Institute of Polar Research, Tachikawa, Japan
[3]The Graduate University for Advanced Studies (SOKENDAI), Tokyo, Japan
[4]Department of Communications and Computer Engineering, Kyoto University, Kyoto, Japan

Correspondence to: Ryosuke Shibuya (shibuya@eps.s.u-tokyo.ac.jp)

Abstract. The first observations made by a complete PANSY radar system (Program of the Antarctic Syowa MST/IS Radar) installed at Syowa Station (39.6° E, 69.0° S) were successfully performed from 16 to 24 March 2015. Over this period, quasi-half-day period (12 h) disturbances in the lower mesosphere at heights of 70 to 80 km were observed. Estimated vertical wavelengths, wave periods and vertical phase velocities of the disturbances were approximately 13.7 km, 12.3 h and $-0.3\,\mathrm{m\,s^{-1}}$, respectively. Under the working hypothesis that such disturbances are attributable to inertia–gravity waves, wave parameters are estimated using a hodograph analysis. The estimated horizontal wavelengths are longer than 1100 km, and the wavenumber vectors tend to point northeastward or southwestward. Using the nonhydrostatic numerical model with a model top of 87 km, quasi-12 h disturbances in the mesosphere were successfully simulated. We show that quasi-12 h disturbances are due to wave-like disturbances with horizontal wavelengths longer than 1400 km and are not due to semidiurnal migrating tides. Wave parameters, such as horizontal wavelengths, vertical wavelengths and wave periods, simulated by the model agree well with those estimated by the PANSY radar observations under the abovementioned assumption. The parameters of the simulated waves are consistent with the dispersion relationship of the inertia–gravity wave. These results indicate that the quasi-12 h disturbances observed by the PANSY radar are attributable to large-scale inertia–gravity waves. By examining a residual of the nonlinear balance equation, it is inferred that the inertia–gravity waves are likely generated

by the spontaneous radiation mechanism of two different jet streams. One is the midlatitude tropospheric jet around the tropopause while the other is the polar night jet. Large vertical fluxes of zonal and meridional momentum associated with large-scale inertia–gravity waves are distributed across a slanted region from the midlatitude lower stratosphere to the polar mesosphere in the meridional cross section. Moreover, the vertical flux of the zonal momentum has a strong negative peak in the mesosphere, suggesting that some large-scale inertia–gravity waves originate in the upper stratosphere.

1 Introduction

Gravity waves are atmospheric waves with a restoring force of buoyancy that can transport momentum upward from the troposphere to the middle atmosphere (e.g., Fritts and Alexander, 2003). Momentum deposition by gravity waves in the mesosphere is a major driving force for the summer-to-winter pole material circulation in the mesosphere (e.g., Plumb, 2002). Adiabatic heating and cooling associated with vertical flow branches of the circulation maintain the thermal structure, which is considerably different from the radiative equilibrium state. Gravity waves also play an essential role in driving the quasi-biennial oscillation (QBO) and semiannual oscillation in the equatorial stratosphere (Sato and Dunkerton, 1997; Haynes, 1998; Baldwin et al., 2003). In addition, it has been shown that gravity wave forcing is essential to the

summer hemispheric low-latitude part of winter stratospheric circulation (Okamoto et al., 2011).

Many observational studies have closely examined characteristics of gravity waves in the troposphere, stratosphere and mesosphere (e.g., Sato, 1994; Sato and Yamada, 1994; Pavelin et al., 2001; Lane et al., 2004; Nastrom and Eaton 2006; Vaughan and Worthington, 2007; Nakamura et al., 1993; Li et al., 2007; Lu et al., 2009; Nicolls et al., 2010; Chen et al., 2013). It is well known that gravity waves have wide spectral ranges of horizontal wavelength from several kilometers to several thousand kilometers and of observed period from several minutes to several hours. Recently, several numerical models directly resolve large parts of gravity wave spectra (the KANTO model, Watanabe et al., 2008; WACCM, Liu et al., 2014; KMCM, Becker, 2009). However, due to their short horizontal wavelengths, many climate models utilize parameterization methods to calculate momentum deposition by unresolved gravity waves (e.g., McFarlane, 1987; Scinocca, 2003; Richter et al., 2009). As parameterization methods involve several tuning parameters related to characteristics of gravity waves, observational constraints on tuning parameters are inevitably required (e.g., Alexander et al., 2010).

Geller et al. (2013) showed that parameterized gravity waves in climate models are not realistic in several aspects in comparison to high-resolution observational data (satellites, isopycnic balloon observations and radiosondes) and gravity-wave-permitting general circulation models. In particular, they showed that gravity wave sources in the parameterization can be poorly specified in high-latitude regions. Such an improper specification of gravity wave sources in southern high-latitude regions is considered to lead several serious problems. One of these problems is the so-called cold-pole bias, present in most climate models in the polar winter stratosphere (Eyring et al., 2010; McLandress et al., 2012). This bias is closely related to significant delays in the breakdown of the stratospheric polar vortex in the Antarctic (Stolarski et al., 2006). Gravity waves in the southern polar region modify formations of polar stratospheric clouds (PSCs), which can enhance ozone depletion in the polar lower stratosphere (Shibata et al., 2003; Watanabe et al., 2006; McDonald et al., 2009; Kohma and Sato, 2011). Moreover, Chu et al. (2011) reported that inertia–gravity waves in the polar mesosphere also affect the formation of polar mesospheric clouds (PMCs). Thus, observational studies of gravity waves around the southern high-latitude region are quite important (e.g., Hertzog et al., 2008).

Recently, a mesosphere–stratosphere–troposphere (MST) radar (or VHF clear-air Doppler radar) system was installed in the Antarctic. The system has completed continuous observations since 30 April 2012 at Syowa Station (69.0° S, 39.6° E) (PANSY (Program of the Antarctic Syowa MST/IS radar) radar; Sato et al., 2014). The radar system provides vertical profiles of three-dimensional winds at high time and height resolutions. The PANSY radar system is a powerful tool for examining gravity waves in the high-latitude region and many other scientific issues related to the polar atmosphere.

One interesting phenomenon observed in the polar mesosphere is a large-amplitude wave-like disturbance with near-inertial frequency (approximately 12 h) that many previous studies have examined (e.g., Murphy et al., 2006; Akmaev et al., 2016). There are several explanations for the existence of such oscillations; Fraser and Khan (1990) and Fisher et al. (2002) posited that these oscillations are attributable to a semidiurnal migrating tide. Waterscheid et al. (1986) and Collins et al. (1992) attributed these oscillations to a "pseudo-tide" mechanism related to gravity-wave momentum deposition modulated by a semidiurnal migrating tide. Hagan and Forbes (2003) investigated the atmospheric response to forcing by zonally asymmetric latent heat release in the troposphere. Talaat and Mayr (2011) found that internal oscillations may be caused by parameterized gravity waves in the model. Other studies (Hernandez et al., 1993; Forbes et al., 1995, 1999; Fritts et al., 1998; Portnyagin et al., 1998; Yamashita et al., 2002; Wu et al., 2003; Aso, 2007; Murphy et al., 2009) suggest that these oscillations are due to semidiurnal non-migrating tides with zonal wavenumber $s = 1$ generated by nonlinear interactions between $s = 1$ stationary planetary waves and semidiurnal migrating tides. Mayr et al. (2005a, b) emphasized the importance of gravity wave filtering effects on nonlinear interactions. Riggin et al. (1999) showed that the zonal wavenumber of the 12 h wave is close to 2 in the winter and is 1 in the summer based on radar observations conducted at McMurdo (77.8° S) and Halley (75.8° S). Wu et al. (2002) suggested that $s = 1$ semidiurnal non-migrating tides are significant at latitudes of higher than 78° and that a mixture of semidiurnal migrating tides and $s = 1$ semidiurnal non-migrating tides appears at between 68° and 78°.

The first successful observation with a complete system of the PANSY radar was performed for 16–24 March 2015. In this study, we used this observational dataset. During this observation period, strong wave-like disturbances with a wave period of about 12 h were found in the lower mesosphere. Using PANSY radar data and a gravity-wave-resolving model, generation and propagation mechanisms of such disturbances were examined. It is suggested that wave-like disturbances with a wave period of about 12 h are attributable to large-scale inertia–gravity waves with horizontal wavelengths of larger than 1100 km.

The present article is organized as follows. The methodology used is described in Sect. 2. Observational results are presented in Sect. 3. The results of the model simulations are given and compared with radar observations in Sect. 4. Propagation characteristics and the wave generation mechanism are also examined. A discussion is presented in Sect. 5, and Sect. 6 summarizes the results and provides concluding remarks.

2 Methodology

2.1 The PANSY radar observations

The PANSY radar system is the first MST/IS radar system installed at Syowa Station ($39.6°$ E, $69.0°$ S) for observing the Antarctic atmosphere in a height region from 1.5 to 500 km. It should be noted that an observation gap exists at a height region from 30 to 60 km due to the lack of the atmospheric radar backscattering in this height region (Sato et al., 2014). The PANSY radar system employs a pulse-modulated monostatic Doppler radar system with an active phased mechanism consisting of 1045 crossed-Yagi antennas. The PANSY radar system is designed to observe three-dimensional winds at a high time resolution and vertical resolution along beam directions of $\Delta t = \sim 1$ min and $\Delta z = 150$ m in the troposphere and lower stratosphere, respectively, and of $\Delta t = \sim 1$ min and $\Delta z = 600$ m in the mesosphere. The accuracy of line-of-sight wind velocity is about $0.1\ \mathrm{m\ s^{-1}}$. As the target of MST radars is atmospheric turbulence, wind measurements can be made under all weather conditions. Continuous observations have been made by the PANSY radar through a partial system since 30 April 2012. The first observation with the complete system of the PANSY radar observation was successfully performed for 16–24 March 2015. See Sato et al. (2014) for further information on the PANSY radar system and for a list of future studies to be conducted based on this system. For the 16–24 March 2015 period, strong polar mesosphere winter echoes, which likely resulted from the largest magnetic storm event occurring during the solar cycle 24 ("St. Patrick's Day storm"; Kataoka et al., 2015; Jacobsen and Andalsvik, 2016; Cherniak and Zakharenkova, 2016), were observed by the PANSY radar system.

The PANSY radar data that we used are line-of-sight wind velocities of five vertical beams tilted east, west, north and south at a zenith angle of $\theta = 10°$. Vertical wind components are directly estimated from the vertical beam. Zonal (meridional) wind components are obtained using a pair of line-of-sight velocities of the east and west beams (the north and south beams). For example, line-of-sight velocities of the east and west beams, $V_{\pm\theta}$, are composed of zonal and vertical components of the wind velocity vectors ($u_{\pm\theta}$, $w_{\pm\theta}$) in the targeted volume ranges:

$$V_{\pm\theta} = \pm u_{\pm\theta}\sin\theta + w_{\pm\theta}\cos\theta.$$

By assuming that the wind field is homogeneous at each height, i.e., $u_{+\theta} = u_{-\theta} \equiv u$ and $w_{+\theta} = w_{-\theta} \equiv w$, we can estimate zonal wind components as

$$u = \frac{V_{+\theta} - V_{-\theta}}{2\sin\theta}.$$

The vertical flux of zonal momentum is directly estimated from variances of line-of-sight wind fluctuations (Vincent and Reid, 1983):

$$\overline{V'^2_{\pm\theta}} = \overline{u'^2_{\pm\theta}}\sin^2\theta + \overline{w'^2_{\pm\theta}}\cos^2\theta \pm \overline{u'_{\pm\theta}w'_{\pm\theta}}\sin 2\theta.$$

By assuming that the flux and variance fields are homogeneous ($\overline{u'^2_{+\theta}} = \overline{u'^2_{-\theta}} \equiv \overline{u'^2}$, $\overline{w'^2_{+\theta}} = \overline{w'^2_{-\theta}} \equiv \overline{w'^2}$ and $\overline{u'_{+\theta}w'_{+\theta}} = \overline{u'_{-\theta}w'_{-\theta}} \equiv \overline{u'w'}$), we obtain

$$\overline{u'w'} = \frac{\overline{V'^2_{+\theta}} - \overline{V'^2_{-\theta}}}{2\sin 2\theta}.$$

This assumption is less strict than that used for the u and w estimates. Thus, the method based on MST radars provides quite accurate estimates of momentum fluxes. The meridional wind component and the vertical flux of meridional momentum can be estimated in a similar manner. Reid and Vincent (1987) examined horizontal wavelengths by using the cross-correlation techniques and the sensitivities of the estimation with several observational periods. In this study, wave parameters are estimated by a hodograph analysis described in Sect. 3.

2.2 Numerical setup for nonhydrostatic model simulation

The simulation was performed using the Nonhydrostatic Icosahedral Atmospheric Model (NICAM), which is a global cloud-resolving model (Satoh et al., 2008, 2014). A nonhydrostatic dynamical core of the NICAM was developed from icosahedral grids modified by the spring dynamics method (Tomita et al., 2002). The NICAM is unique in its use of a flux-form nonhydrostatic equation system that assures the conservation of total mass, momentum and energy over the domain.

2.2.1 Horizontal and vertical coordinate system

Resolutions of horizontal icosahedral grids are represented by glevel n (grid division level n). Glevel 0 denotes the original icosahedron. By dividing each triangle into four small triangles recursively, one-higher resolution is obtained. The total number of grid points is $N_g = 10 \cdot 4^n + 2$ for glevel n. The actual resolution corresponds to the square root of the averaged control volume area, $\Delta x \equiv \sqrt{4\pi R_E^2 / N_g}$, where R_E is the Earth's radius. A glevel-7 grid is used in this study ($\Delta x \sim 56$ km).

Recently, Shibuya et al. (2016) developed a new grid configuration for quasi-uniform and regionally fine meshes within a circular region with icosahedral grids using spring dynamics. This method clusters grid points over the sphere into the circular region (the targeted region) and realizes finer meshes than original icosahedral grids. By introducing sets of mathematical constraints, it has been shown that the minimum resolution within the targeted region is uniquely determined by the area of the targeted region alone. In this study, the targeted region for a given glevel is a region south of $30°$ S centered at the South Pole. Figure 1a shows an illustration of the stretched grid which is roughened up to glevel 3. Figure 1b shows a horizontal map of a normalized grid
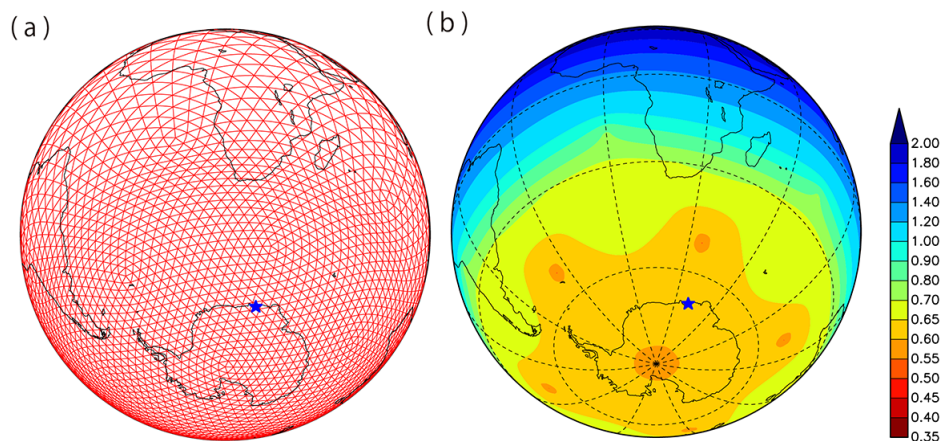
Figure 1. (a) An illustration of the stretched grid (roughened up to glevel 3). **(b)** A horizontal map of a normalized grid interval defined as $d/\Delta x$, where d denotes grid intervals and Δx denotes the grid interval of the original icosahedral grid.

interval defined as $d(\lambda\phi)/\Delta x$, where d denotes grid intervals as a function of the longitude, λ, and the latitude, ϕ. In this case, the horizontal resolution in the targeted region is roughly 36 km.

To simulate structures of disturbances from the stratosphere to the mesosphere, the vertical grid spacing is 400 m at heights from 2.4 to 80 km. It should be noted that according to Watanabe et al. (2015), gravity wave momentum flux is not heavily dependent on model vertical spacing in the middle atmosphere when $\Delta z < 400$ m. The number of vertical grids is 217. To prevent unphysical waves reflection at the top of the boundary, a 7 km thick sponge layer is set above $z = 80$ km. The second-order Laplacian horizontal hyperviscosity diffusion and Rayleigh damping for the vertical velocity are used for the sponge layer. An e-folding time of the ∇^2 horizontal diffusion for the $2\Delta x$ wave at the top of the model is 4 s, and an e-folding time of the Rayleigh damping for the vertical velocity for the top of the model is 216 s. The diffusivity level gradually increases from the bottom to the top of the sponge layer. We confirm that little wave reflection near the sponge layer occurs under this setting (not shown).

2.2.2   Initial condition and other physical schemes

MERRA reanalysis data based on the Goddard Earth Observing System Data Analysis System, Version 5 (GEOS-5 DAS; Rienecker et al., 2011), are used as the initial condition. In the MERRA reanalysis data, the following two types of 3-D fields are provided: one set is produced through the corrector segment of the Incremental Analysis Update (IAU; Bloom et al., 1996) cycle ($1.25° \times 1.25°$ and 42 vertical levels whose top is 0.1 hPa) and the other pertains to fields resulting from Gridpoint Statistical Interpolation analyses (GSI analysis; e.g., Wu et al., 2002) on the native horizontal grid and on native model vertical levels ($0.75° \times 0.75°$ and 72 vertical levels whose top is 0.01 hPa). We use the former 3-D assimilated fields for 1000 to 0.1 hPa and the latter 3-D an-

alyzed fields for 0.1 to 0.01 hPa for the initial condition of the NICAM simulation to prepare realistic atmospheric fields in the mesosphere for 00:00 UTC on 17 March 2015. The latter 3-D analyzed fields were only used at above 0.1 hPa, as variables of vertical pressure velocity, cloud liquid water and ice mixing ratios are not included. Vertical pressure velocities, cloud liquid water and ice mixing ratios above 0.1 hPa are set to zero. A time integration was performed until 00:00 UTC on 24 March. The time step was 15 s. As part of the boundary layer scheme, MYNN level 2 (Nakanishi and Niino, 2004) was used. No cumulous or gravity wave parameterization was employed. The model output was recorded every 1 h. It should be noted that this model does not use the nudging method as an external forcing for the atmospheric component.

3   Observational results

Figure 2a shows the time–height section of the line-of-sight wind velocity observed by the east beam of the PANSY radar system. In the lower stratosphere, wavy structures with short vertical wavelengths are shown. Shibuya et al. (2015) showed that such a structure observed in May of 2013 at Syowa Station was due to inertia–gravity waves with a vertical wavelength of about 2 km. In the mesosphere, strong echoes were detected at heights of 60 to 80 km over this time period. These polar mesosphere winter echoes (PMWEs) are likely initiated by increased ionization during the solar flare event occurring on 17–18 March 2015 (Kataoka et al., 2015; Jacobsen and Andalsvik, 2016; Cherniak and Zakharenkova, 2016). In this period, the polar night jet was in the phase of formation around Syowa Station at the stratopause (at the height of about 55 km; not shown). As is shown in Fig. 2a, strong wave-like disturbances were observed in the mesosphere. Figure 2b and c show line-of-sight wind velocities of the east and west beams, respectively, at heights of 65–80 km
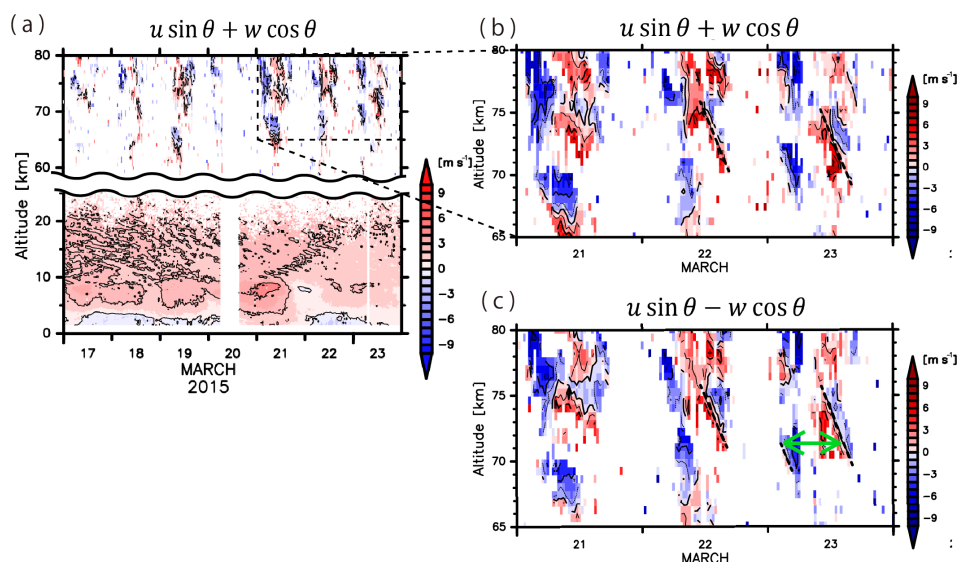
Figure 2. Time–altitude cross sections of eastward line-of-sight velocity components observed by the PANSY radar at Syowa Station **(a)** for the period from 17 to 23 March 2015, **(b)** for the period from 21 to 23 March 2015 and **(c)** opposite of westward line-of-sight velocity components observed by the PANSY radar for the period from 21 to 23 March 2015. The dashed line in **(b)** and **(c)** denotes phase lines with the downward phase velocity of $0.3\,\mathrm{m\,s^{-1}}$. The green arrows in **(c)** denotes the wave period of the disturbance. The contour intervals are $2\,\mathrm{m\,s^{-1}}$.

for 00:00 UTC on 21 March to 00:00 UTC on 24 March. In Fig. 2b and c, it is clear that phases of dominant disturbances propagate downward; a vertical phase velocity (broken line) and an observed period (a green arrow) are about $-0.3\,\mathrm{m\,s^{-1}}$ and 12.3 h, respectively. This indicates that the vertical wavelength is about 13.8 km.

As the zenith angle of tilted beams of the PANSY radar system is $\theta = 10°$, locations of the observation points by opposite beams in the mesosphere are separated by approximately 25 km at a height of 70 km. Figure 3a and b show time–height sections of estimated zonal and meridional wind components.

Based on the working hypothesis that wind disturbances in the mesosphere are due to inertia–gravity waves, wave parameters are estimated using a hodograph analysis. A hodograph analysis (e.g., Hirota and Niki, 1986; Sato, 1994) is applied to wind fluctuations at heights of 73.2, 73.8 and 74.4 km for 22 March and at the heights of 70.8, 71.4 and 72.0 km for 23 March. In this analysis, hodographs are made in the time direction.

First, wave zonal (u') and meridional (v') wind fluctuations were fitted to sinusoidal functions as follows:

$$u' = \hat{u}\sin(\omega t + \theta_u) + u_\mathrm{o}$$
$$v' = \hat{v}\sin(\omega t + \theta_v) + v_\mathrm{o}, \qquad (1)$$

where $\hat{u}$ and $\hat{v}$ are the amplitudes of u' and v', respectively, ω is the observed wave frequency, t is time, θ_u and θ_v are phases of zonal and meridional wind fluctuations, and u_o and v_o are offsets of zonal and meridional wind fluctuations, respectively. Parameters ($\hat{u}$, $\hat{v}$, ω, θ_u, θ_v, u_o and v_o)
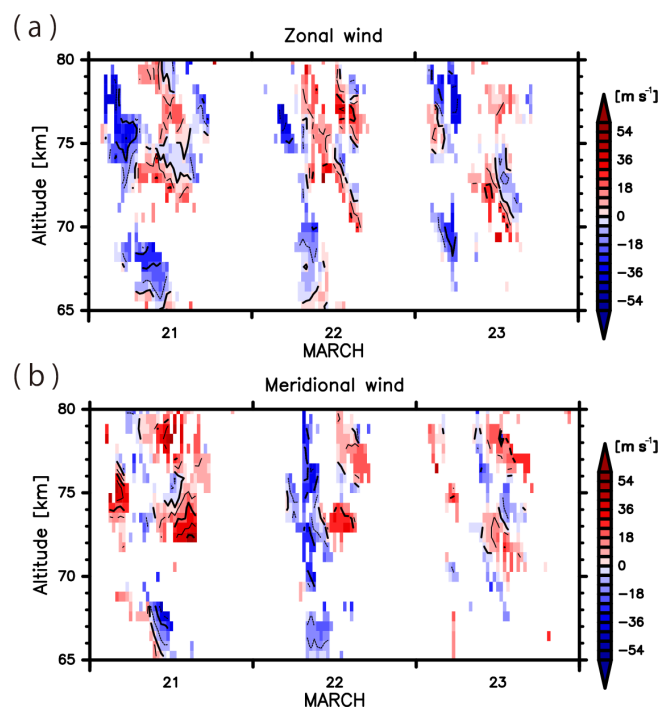
Figure 3. Time–altitude cross sections of **(a)** zonal wind components and **(b)** meridional wind components observed by the PANSY radar at Syowa Station for the period from 21 to 23 March 2015. The contour intervals are $12\,\mathrm{m\,s^{-1}}$.

Table 1. The wave parameters of fluctuations in the mesosphere observed over Syowa Station **(a)** obtained by fitting to a sinusoidal function using a nonlinear least-squares method and **(b)** estimated on the hypothesis that fluctuations are due to inertia–gravity waves, where α is the angle of $u_\parallel$ measured clockwise from the east. The error bar is based on the uncertainty by using a nonlinear least-squares method.

(a) Time and height locations	ω (s^{-1})	m (m^{-1}) from u'	C_{p_z} (m s^{-1}) from u'	m (m^{-1}) from v'	C_{p_z} (m s^{-1}) from v'
3/22 73.2 km	1.42×10^{-4} (12.3 h)	5.24×10^{-4} (12.0 km)	-0.26	7.42×10^{-4} (8.47 km)	-0.19
3/22 73.8 km	1.27×10^{-4} (13.7 h)				
3/22 74.4 km	1.59×10^{-4} (11.0 h)				
3/23 70.8 km	1.35×10^{-4} (12.9 h)	4.08×10^{-4} (15.4 km)	-0.34	5.11×10^{-4} (12.3 km)	-0.28
3/23 71.4 km	1.35×10^{-4} (12.9 h)				
3/23 72.0 km	1.42×10^{-4} (12.3 h)				

(b) Time and height locations	u' (m s^{-1})	v' (m s^{-1})	$\lvert 2\pi/k_h \rvert$ (km)	α (degree)	$\dfrac{f}{\hat{\omega}}$
3/22 73.2 km	28.5 ± 2.8	21.3 ± 2.8	1775 (1207–2797)	12° (7–32°)	0.72 (0.57–0.85)
3/22 73.8 km	30.3 ± 4.5	27.0 ± 4.5	3238 (1577–3407)	18° (5–77°)	0.86 (0.63–0.87)
3/22 74.4 km	28.3 ± 5.9	29.3 ± 5.9	1790 (1118–1793)	48° (17–75°)	0.76 (0.59–0.76)
3/23 70.8 km	32.2 ± 4.8	22.8 ± 4.8	1785 (990–7778)	2° (1–52°)	0.56 (0.41–0.97)
3/23 71.4 km	28.7 ± 6.1	22.1 ± 6.1	1454 (870–1523)	14° (11–61°)	0.63 (0.41–0.65)
3/23 72.0 km	39.0 ± 8.0	23.8 ± 8.0	1150 (570–1914)	14° (10–47°)	0.70 (0.32–0.74)

are determined using a nonlinear least-squares method so that the residual $\sqrt{(u'_{\text{obs}} - u')^2 + (v'_{\text{obs}} - v')^2}$ is smallest. Figure 4 shows a time series of observed horizontal wind fluctuations and results of the fitting at 70.8 and 72.0 km for 23 March. It is clear that the observed wind fluctuations seem to have a sinusoidal form with a period of about 12 h, and the fitting is successful. Moreover, phases of zonal and meridional wind fluctuations at 72.0 km seem to be advanced compared to those at 70.8 km. Using these phase differences in zonal and meridional wind fluctuations, vertical wavenumbers for zonal and meridional fluctuations are estimated, respectively. Table 1a summarizes parameters such as wave frequencies, vertical wavenumbers and vertical phase velocities estimated from u' and v'. The estimated period ranges from 11.0 to 13.8 h, which is quasi-12 h. The estimated vertical wavelengths are 12.0 and 8.5 km for u' and v' for 22 March and are 15.4 and 12.3 km for u' and v' for 23 March, respectively. Thus, the vertical phase velocities are -0.26 and -0.19 m s^{-1} for u' and v' for 22 March and -0.35 and -0.28 m s^{-1} for u' and v' for 23 March, respectively. Although the estimation based on v' for 22 March shows slightly different values, the vertical phase velocities and observed periods agree well with the rough estimation denoted by broken lines and the green arrow in Fig. 2b and c, respectively (approximately -0.3 m s^{-1} and 12.3 h).

The linear theory of inertia–gravity waves indicates that a hodograph is ellipse-shaped (e.g., Shibuya et al., 2015). The lengths of major and minor axes of the hodograph ellipse correspond to the amplitudes of horizontal wind components, which are parallel ($u_\parallel$) and orthogonal ($u_\perp$) to the horizontal wavenumber vector ($\boldsymbol{k}_h$), respectively. The components of $u_\parallel$ and $u_\perp$ are written using the zonal (u') and meridional (v')

wind fluctuations:

$$u_\parallel = u' \cos\alpha + v' \sin\alpha$$
$$u_\perp = -u' \sin\alpha + v' \cos\alpha, \qquad (2)$$

where α is the angle of $u_\parallel$ measured clockwise from the east. Based on the polarization relation, the intrinsic frequency $\hat{\omega}$ can be determined from the ratio of the lengths of the major to minor axes:

$$\hat{\omega} = \left| \frac{u_\parallel}{u_\perp} f \right|, \qquad (3)$$

where f denotes the inertial frequency. The intrinsic frequency is taken to be positive without losing generality (e.g., Sato et al., 1997).

The direction of the vertical energy propagation can be estimated from the rotation of the hodograph in the vertical direction as follows: in the Southern Hemisphere, a counterclockwise (clockwise) rotation with increasing height denotes upward (downward) energy propagation. Hodographs in the vertical direction for 12:00 UTC on 22 March and for 12:00 UTC on 23 March show counterclockwise rotation (not shown), indicating upward energy propagation as also shown in Fig. 4. This also means that the vertical wavenumber m is negative.

The horizontal wavenumber $\lvert \boldsymbol{k}_h \rvert$ can be indirectly estimated using the dispersion relation of inertia–gravity waves, though an ambiguity for 180° remains in the direction of the horizontal wavenumber vector. For hydrostatic inertia–gravity waves, the dispersion relation in a uniform background is written as follows:

$$\lvert \boldsymbol{k}_h \rvert = \sqrt{\frac{(\hat{\omega}^2 - f^2)\, m^2}{N^2}}, \qquad (4)$$

where N is the Brunt–Väisälä frequency. Here, as a typical value, $N^2 = 3.0 \times 10^{-4}$ s^{-2} for the mesosphere was used. The
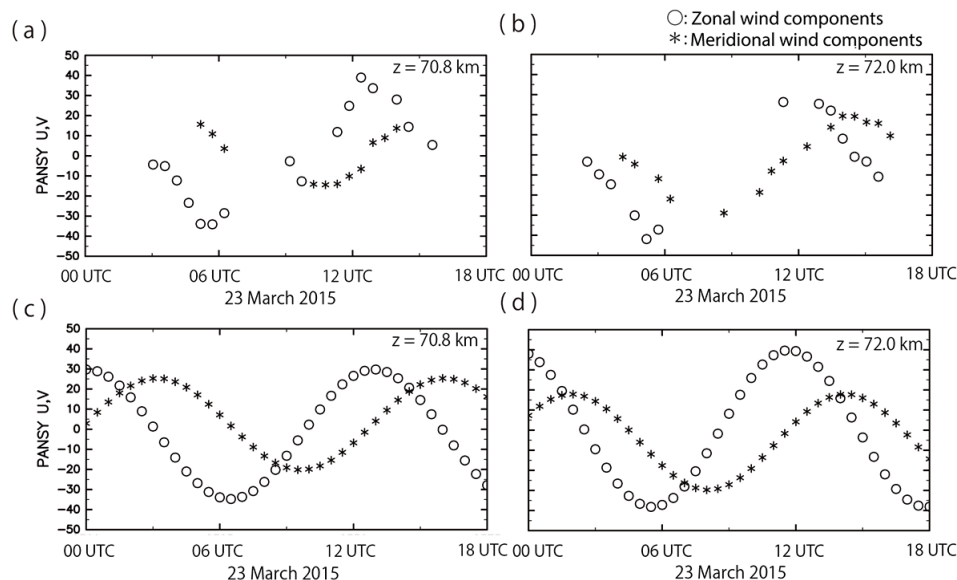
Figure 4. Zonal and meridional wind components observed by the PANSY radar on 23 March 2015 as a function of time at heights of (**a**) 70.8 km and (**b**) 72.0 km. Zonal and meridional wind components fitted sinusoidal functions using a nonlinear least-squares method at the height of (**c**) 70.8 km and (**d**) 72.0 km. The circles denote the zonal wind components and the star marks denote the meridional components.
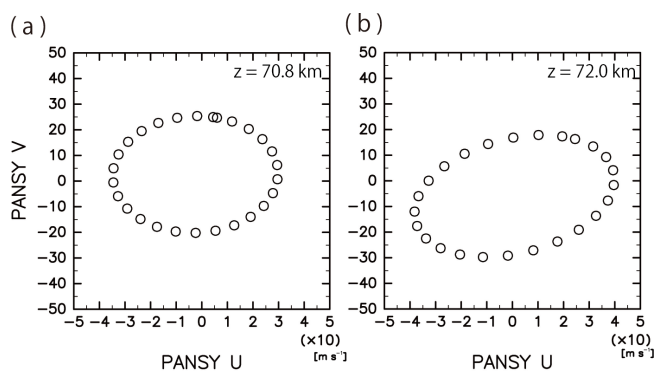
Figure 5. A hodograph of the fitted horizontal wind components in the time region from 00:00 UTC to 13:00 UTC, 23 March, at the height of (**a**) 70.8 km and (**b**) 72.0 km from the PANSY radar observation. Each mark is plotted at one hour interval.

zonal and meridional wavenumbers (k, l) are determined as $k = \pm |\mathbf{k}_h| \cos \alpha$ and $l = \pm |\mathbf{k}_h| \sin \alpha$, respectively. The plus–minus sign here denotes the ambiguity of the wavenumber vector.

Figure 5 shows hodographs of the fitted sinusoidal fluctuations at heights of 70.8 and 72.0 km for 23 March. The intrinsic frequency and zonal and meridional wavenumbers are estimated from Eqs. (3) and (4), respectively. Table 1b presents the fitted amplitude of zonal and meridional wind fluctuation and estimated wave parameters resulting from the hodograph analysis. Wavenumbers are directed eastward (or westward) or northeastward (or southwestward). Parameter $f / \hat{\omega}$ ranges from 0.6 to 0.85. Horizontal wavelengths of the best-

fitted parameters are longer than 1100 km, indicating that these fluctuations are due to relatively large-scale inertia–gravity waves. Thus, the applied assumption on the homogeneity of observed winds by dual beams (Sect. 2.1) is justified. Uncertainties of estimated wind amplitude and other related wave parameters are also estimated using residuals of the nonlinear least-squares fitting and on the assumption that the uncertainties in the estimates of the zonal and meridional wind amplitude are the same. It seems that the estimated horizontal wavelength at a height of 70.8 km for 23 March has a relatively large uncertainty ($|2\pi/\mathbf{k}_h| = 990 \sim 7778$ km). However, it should be noted that the case for the largest horizontal wavelength corresponds to a case with $\hat{\omega} \sim f$ (i.e., close to the inertial oscillation) and hence its ambiguity is large for the wavelength ($|\mathbf{k}_h| \sim 0$).

4 Numerical experiment results

4.1 Simulated wave structures

To examine spatial structures and generation mechanisms of the inertia–gravity waves, a model simulation based on the NICAM was performed. Figure 6a shows the time–height section of the simulated winds ($u \sin \theta + w \cos \theta$ (where $\theta = 10°$)) for Syowa Station from 00:00 UTC on 17 March to 00:00 UTC on 24 March 2015, reflecting the line-of-sight velocity of the east beam of the PANSY radar system. A comparison with the observations (Fig. 2) shows that the model successfully simulated synoptic-scale disturbances in the troposphere, although phases of these disturbances vary slightly from observations near the end of
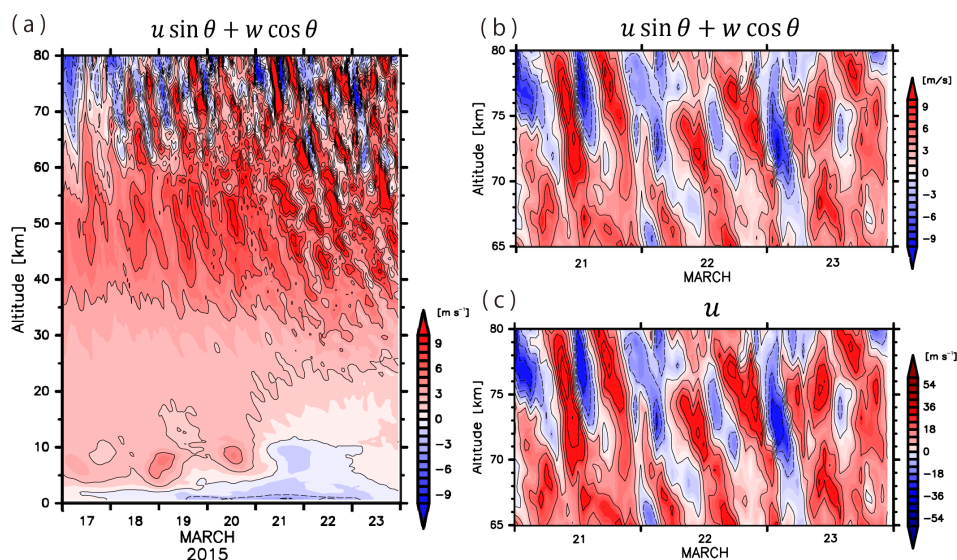
Figure 6. Time–altitude cross sections of eastward line-of-sight velocity components simulated by NICAM at Syowa Station **(a)** for the period from 17 to 23 March 2015 and **(b)** for the period from 21 to 23 March 2015 (contour interval $3\,\mathrm{m\,s^{-1}}$). **(c)** Zonal wind components in eastward line-of-sight velocity components simulated by NICAM for the period from 21 to 23 March 2015 (contour interval $18\,\mathrm{m\,s^{-1}}$).

the simulation. In the lower stratosphere, a wavy structure with a small vertical wavelength of less than about 2 km, which was observed by the radar system from 00:00 UTC on 17 March to 00:00 UTC on 20 March, is hardly shown in Fig. 6a. This may be attributable to the large vertical spacing ($\Delta z = 400\,\mathrm{m}$) of the model compared to such a short vertical wavelength. From the middle stratosphere to the mesosphere, downward-propagating large-amplitude disturbances are dominant, which is consistent with the observations. Figure 6b and c show the line-of-sight velocity of the east beam and the zonal wind component for the same time and height sections as those reflected in Fig. 2b and c, respectively. The amplitude of these disturbances is also comparable to that of the observations; for example, the amplitude of the zonal wind component at a height of about 70 km for 12:00 UTC on 23 March is approximately $30\,\mathrm{m\,s^{-1}}$, which agrees with the observations (see Fig. 4a and c).

Figure 7a shows the time–height section of anomalies of zonal wind components from the time average at each height. As is shown in Fig. 6b, wave-like structures for the observation period of about 12 h seem dominant in the mesosphere, which is consistent with the radar observation (Fig. 2b). Thus, we first examined diurnal and semidiurnal migrating tidal components, which are defined as components for wave period $\tau = 24\,\mathrm{h}$ and zonal wavenumber $s = 1$ and for $\tau = 12\,\mathrm{h}$ and $s = 2$, respectively. Figure 7b shows the time–height section of diurnal and semidiurnal migrating components of zonal winds. Surprisingly, these components are not dominant even in the mesosphere. Figure 7c shows the time–height section of zonal wind components of planetary wave components, which are defined as components with $\tau \geq 42\,\mathrm{h}$. This component does not seem to be dominant

in the mesosphere. Moreover, we examined the amplitude of small-scale gravity waves, which are defined as components with horizontal wavelengths of less than 1000 km, as occasionally shown by previous studies (e.g., Geller et al., 2013). In this study, a spatial filter is applied to the x–y coordinate centered at the South Pole as projected by the Lambert azimuthal equal-area projection. Figure 7d shows the time–height section of zonal wind components of the small-scale gravity waves. Although these small-scale gravity waves sometimes have amplitudes that exceed $20\,\mathrm{m\,s^{-1}}$ in the mesosphere, the wave structures shown in Fig. 7a are not fully explained.

The remaining component is shown in Fig. 7e. This component has a quite similar structure and amplitude to the unfiltered anomalies shown in Fig. 7a. These results suggest that dominant wave structures in the mesosphere did not form due to migrating tides, planetary waves or small-scale gravity waves but rather due to the remaining component. The remaining component has a horizontal wavelength of greater than 1000 km and wave periods of less than 42 h. We further examined characteristics of the remaining component such as horizontal and vertical wavenumbers and intrinsic and observed wave frequencies.

Figure 7e shows several large-amplitude wave packets over Syowa Station. The envelope function of the wave packets is examined using an extended Hilbert transform method proposed by Sato et al. (2013). An extended Hilbert transform $H\,[a\,(x,t)]$ is a fluctuation field composed of a Fourier component of a particular fluctuation field $a(xt)$ whose phase is shifted by $-\pi\,/\,2$ radians. An envelope function $A_{\mathrm{env}}(xt)$
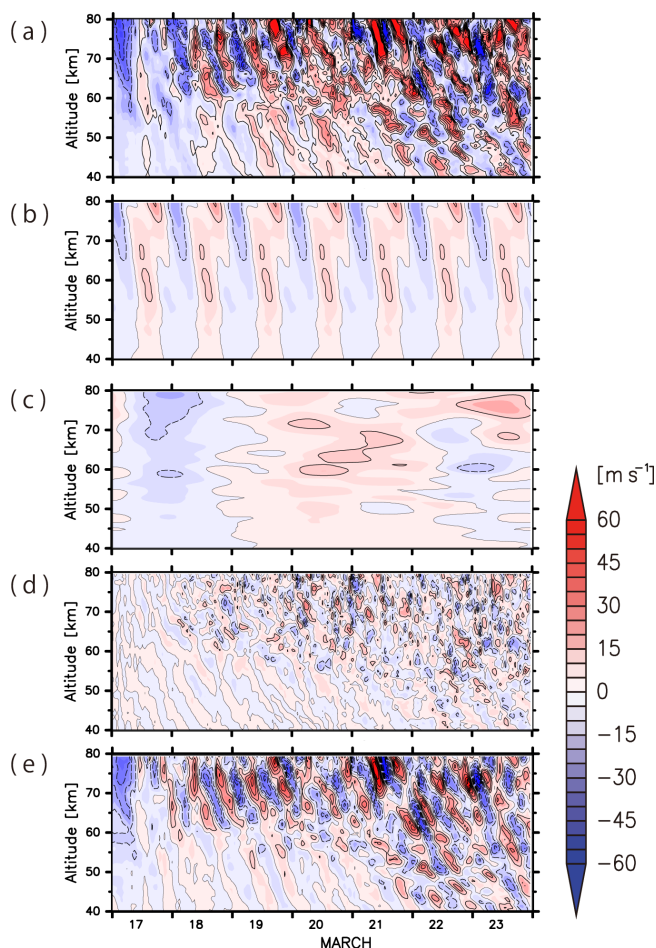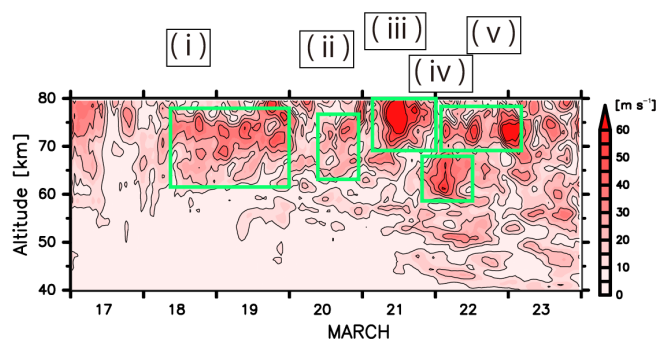
Figure 7. Time–altitude cross sections of (a) anomalies of the zonal wind components from the time–mean components, (b) the diurnal and semidiurnal migrating tidal components, (c) the planetary wave components, (d) small-scale gravity waves and (e) the remaining components. The contour intervals are $10\,\mathrm{m\,s^{-1}}$. The data are from the NICAM simulation.

Figure 8. Time–altitude cross section of the envelope function of the zonal wind components of the large-scale gravity waves simulated by NICAM (contour interval $10\,\mathrm{m\,s^{-1}}$). (i) to (v) denote the labels of the wave packet examined in Sect. 4.

Figure 9. Hovmöller diagram of zonal wind components of the large-scale inertia–gravity waves simulated by NICAM at the height of 70 km at 69° S (contour interval $10\,\mathrm{m\,s^{-1}}$). (i), (ii) and (v) indicate the packets labeled in Fig. 5.
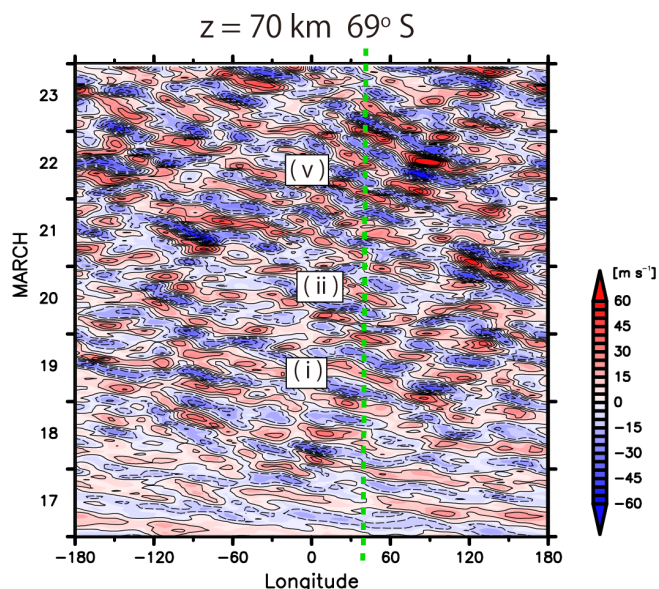
of $a(xt)$ is obtained using $a(xt)$ as follows:

$$A_{\mathrm{env}}(x,t) = \sqrt{a(x,t)^2 + H[a(x,t)]^2}. \tag{5}$$

The extended Hilbert transform must be applied in one direction in time or space where waves are fluctuating (including at least more than two wave crests). In this study, envelope functions are estimated using the extended Hilbert transform of the time direction.

Figure 8 shows the envelope functions calculated using the extended Hilbert transform applied to remaining components shown in Fig. 7e. Several large-amplitude wave packets are identified and labeled as (i) to (v) for further wave parameter estimation. The observed wave period and the vertical wavelength of each packet are estimated directly in Fig. 7e. The zonal wavelengths and phase velocities are directly estimated using Hovmöller diagrams. Figure 9 shows the Hovmöller diagram at a height of 70 km at 69° S. A lot of wave

packets appear not only over Syowa Station throughout the simulation period, except for the initial day of the time integration. It is clear that most waves propagate westward. At a longitude of roughly 40° E (green dashed line) where Syowa Station is located, some dominant wave packets are found as is shown in Fig. 8, corresponding to packets (i) for 19 March, (ii) 20 March and (v) 22 March, respectively.

In addition, to examine horizontal structures of the wave packets, we created composite maps of zonal wind components. The composite is calculated for the time period denoted by green rectangles in Fig. 8. For each wave packet, the locations with the local maxima of the zonal wind components near Syowa Station along a latitude of 69° S are chosen as reference points for the composite. In other words,
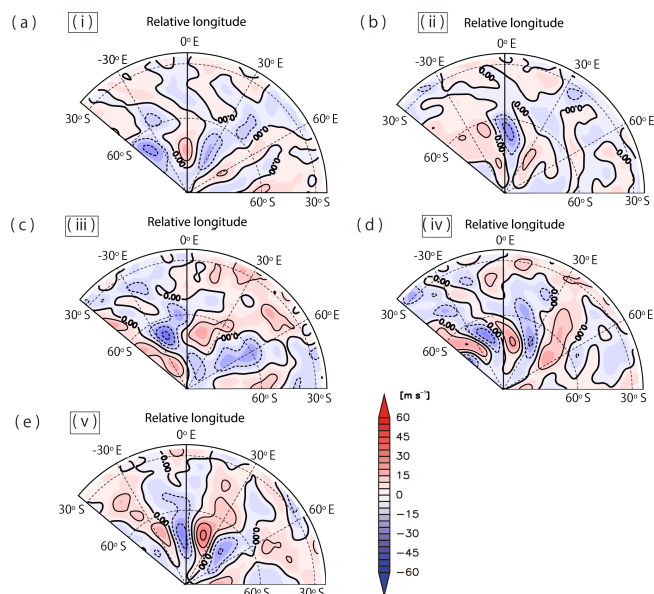
Figure 10. Composite maps of zonal wind components of the large-scale inertia–gravity waves simulated by NICAM. The height where the composites are taken is **(a)** 70 km, **(b)** 70 km, **(c)** 75 km, **(d)** 65 km and **(e)** 72 km. The longitudinal location is depicted as the relative longitude from Syowa Station. The contour intervals are 10 m s^{-1}.

horizontal maps of zonal wind wave components are moved in the zonal direction and are then averaged. Thus, this composite shows an averaged phase structure of zonal wind wave components near Syowa Station. The results are shown in Fig. 10a to e for packets (i) to (v), respectively. It seems that wave structures are evident for all packets near Syowa Station. From features observed in the time–height section, the Hovmöller diagram and the composite maps of zonal wind components, we directly estimated wave parameters of horizontal wavelengths, vertical wavelengths, observed frequencies, zonal phase speeds, vertical phase speeds and intrinsic frequencies, which are summarized in Table 2.

The vertical phase speeds, observed wave periods and vertical wavelengths obtained from the model simulation data agree quite well with those obtained from the PANSY radar observations. Moreover, directly estimated zonal and meridional wavenumbers from the simulation (Table 2) also agree quite well with those indirectly estimated from PANSY radar observations using polarization and dispersion relations of inertia–gravity waves (Table 1a and b). In addition, it is important to note that wave parameters (ω, $\boldsymbol{k}$ and m) of packets (i) to (v) are consistent with the dispersion relation of the hydrostatic inertia–gravity waves:

$$\hat{\omega}^2 = (\omega - \boldsymbol{U} \times \boldsymbol{k})^2 = f^2 + \frac{N^2 |\boldsymbol{k}|^2}{m^2}, \tag{6}$$

where ω is the ground-based frequency, $\boldsymbol{k} = (k, l)$ and m are horizontal and vertical components for the wavenumber vec-

tor, respectively, and $\boldsymbol{U}$ is the background horizontal wind vector. Intrinsic frequencies $\hat{\omega}$ obtained from the model simulation using Eq. (6) also agree with those obtained from the PANSY radar observation. From these results, we conclude that dominant half-day wave period fluctuations observed in the mesosphere are likely attributable to large-scale inertia–gravity waves. Hereafter, we refer to the remaining component as "large-scale inertia–gravity waves".

4.2 Wave propagation and generation mechanism

In this section, we examine the origins of the large-scale inertia–gravity waves simulated near Syowa Station. In particular, we examine disturbances occurring over wave periods of close to 12 h, which were extracted by applying a bandpass filter with cutoff wave periods of 6 and 24 h to large-scale inertia–gravity waves. It is confirmed that this spectral range of the bandpass filter is narrow enough to extract the large-scale inertia–gravity waves clearly.

Case studies are conducted for wave packets (i) and (v), as they show clear wave structures at the height of 70 km, where the PANSY radar system observed inertia–gravity waves. The propagation of wave packets identified using the extended Hilbert transform method is manually traced. Three-dimensional locations of the wave packets are determined by the maxima of the envelope function for each time. Hereafter, we refer to this method as "manual wave packet tracing". The advantage of this method is that a specific location of a possible wave source can be directly examined.

The approach of the manual wave packet tracing for packet (v) is illustrated in Fig. 11a and b, which show horizontal maps of zonal wind components of the large-scale inertia–gravity waves and their envelope functions for 03:00 UTC on 23 March and a Hovmöller diagram at 69° S. Significant wave disturbances with large amplitudes are observed near Syowa Station, corresponding to packet (v). The location of packet (v) (green circles in Fig. 11a and b) is estimated in the following: first, the time when the envelope function of packet (v) takes its local maximum in the Hovmöller diagram (Fig. 11b) is determined. Second, the location of packet (v) at that time is determined to where the envelope function has its local maximum in the horizontal map (Fig. 11a). Figure 11c and d show the results for packet (i). By repeating this procedure at an interval of about 1 km in the vertical direction, temporal and spatial locations for a particular packet are manually estimated. For this tracing, the Hovmöller diagram is examined at the latitude of the wave packet location in the former procedure.

Figure 12a–d show the time and the spatial locations of packet (v) at heights of 60, 40, 25 and 23 km, respectively. It appears that the location of packet (v) is successfully traced backward from a height of 70 to 23 km, suggesting that packet (v) observed over Syowa Station in the mesosphere propagated from the lower stratosphere at roughly (100° E, 40° S). At heights of 25 to 23 km, the vertical propagation of

Table 2. The directly estimated wave parameters of simulated packets.

Wave packets	k (m^{-1})	l (m^{-1})	m (m^{-1})	ω (s^{-1})	C_{p_x} (m s^{-1})	C_{p_z} (m s^{-1})	$\frac{f}{\omega}$
		$|k_h|$ (m^{-1})					
(i) $z = 70$ km 3/18 12 UTC–3/19 24 UTC	-2.48×10^{-6} (2530 km)	~ 0	3.96×10^{-4} (15.8 km)	1.42×10^{-4} (12.3 h)	-57.3	-0.36	0.763
		2.48×10^{-6} (2530 km)					
(ii) $z = 70$ km 3/20 05 UTC–3/21 01 UTC	-3.18×10^{-6} (1980 km)	-0.98×10^{-6} (6440 km)	4.10×10^{-4} (15.3 km)	1.47×10^{-4} (11.8 h)	-4.62	-0.36	0.704
		3.33×10^{-6} (1887 km)					
(iii) $z = 75$ km 3/21 03 UTC–3/22 03 UTC	-2.79×10^{-6} (2250 km)	-2.48×10^{-6} (2530 km)	3.92×10^{-4} (16.0 km)	1.99×10^{-4} (8.8 h)	-71.3	-0.51	0.617
		3.73×10^{-6} (1685 km)					
(iv) $z = 65$ km 3/21 21 UTC–3/22 09 UTC	-3.35×10^{-6} (1880 km)	-2.78×10^{-6} (2530 km)	4.63×10^{-4} (13.57 km)	1.46×10^{-4} (11.9 h)	-43.5	-0.32	0.617
		4.35×10^{-6} (1444 km)					
(v) $z = 72$ km 3/22 02 UTC–3/23 02 UTC	-3.78×10^{-6} (1660 km)	-0.82×10^{-6} (7660 km)	4.52×10^{-4} (13.9 km)	1.59×10^{-4} (11.0 h)	-42.1	-0.35	0.653
		3.87×10^{-6} (1625 km)					

packet (v) is quite slow compared to that in the upper stratosphere and mesosphere.

Figure 12e to g show the times and spatial locations of packet (i) at heights of 63, 58, 53 and 48 km, respectively. At heights of 70, 63 and 58 km, the green circles seem to trace the same wave structures. However, as we cannot trace packet (i) below a height of 53 km, the wave structure becomes obscured at heights of 53 and 48 km.

To confirm the validity of the manual wave packet tracing results, we conducted a backward ray tracing analysis of the large-scale inertia–gravity wave (e.g., Marks and Eckermann, 1995). We used the wave parameters of packets (i) and (v) shown in Table 2 as initial parameters for the ray tracing analysis. The average of the model output for 17 to 23 March is used as the background wind for the ray tracing analysis. Figure 13 and Table 3 summarize the manual packet and ray tracing results. The times and spatial locations of packet (v) detected by the manual packet tracing agree with those obtained by idealized ray tracing, although not for the lower stratosphere. However, the tracing of packet (i) agrees with those by idealized ray tracing results at above 58 km where clear wave structures are shown in the horizontal map, although the idealized ray slowly travels at right angles to the manual ray. These findings support the validity of manual wave packet tracing based on the extended Hilbert transform and ray tracing based on inertia–gravity wave theory.

The source of the inertia–gravity waves can be located at any altitude along the ray above the lowest traceable altitude. Thus, we further examine possible sources of packets (i) and (v) along the ray shown in Fig. 13. First, we focus on the ray of packet (v) in the lower stratosphere. Figure 14 shows the longitude–height section of background winds below $z = 18$ km and of disturbances above $z = 19$ km at 40° S for 03:00 UTC on 21 March. At roughly 100° E longitude, wave disturbances appear to be captured over the core of the tropospheric jet stream. This feature is quite similar to the gravity waves generated by the spontaneous radiation from the large-scale jet in the tropopause (e.g., O'Sullivan and Dunkerton, 1995; Plougonven and Synder, 2007; Yasuda et al., 2015a, b). The long propagation time in the lower stratosphere may be related to the wave-capture mechanism (Bühler and McIntyre, 2005; Shibuya et al., 2015).

To explore such a possibility, a horizontal map of the residual of the nonlinear balance equation (ΔNBE; Zhang et al., 2001), which is an index showing the degree of flow imbalance, is examined. Here, ΔNBE is defined as follows:

$$\Delta\mathrm{NBE} = 2J(u, v) + f\varsigma - \alpha\nabla^2 P, \qquad (7)$$

where ς, α and P denote the relative vorticity, specific volume and pressure level, respectively. The Jacobian term is $J(u, v) = \partial u\,/\,\partial x \times \partial v\,/\,\partial y - \partial v\,/\,\partial x \times \partial u\,/\,\partial y$. To exclude possible contaminations of ΔNBE by small-scale gravity
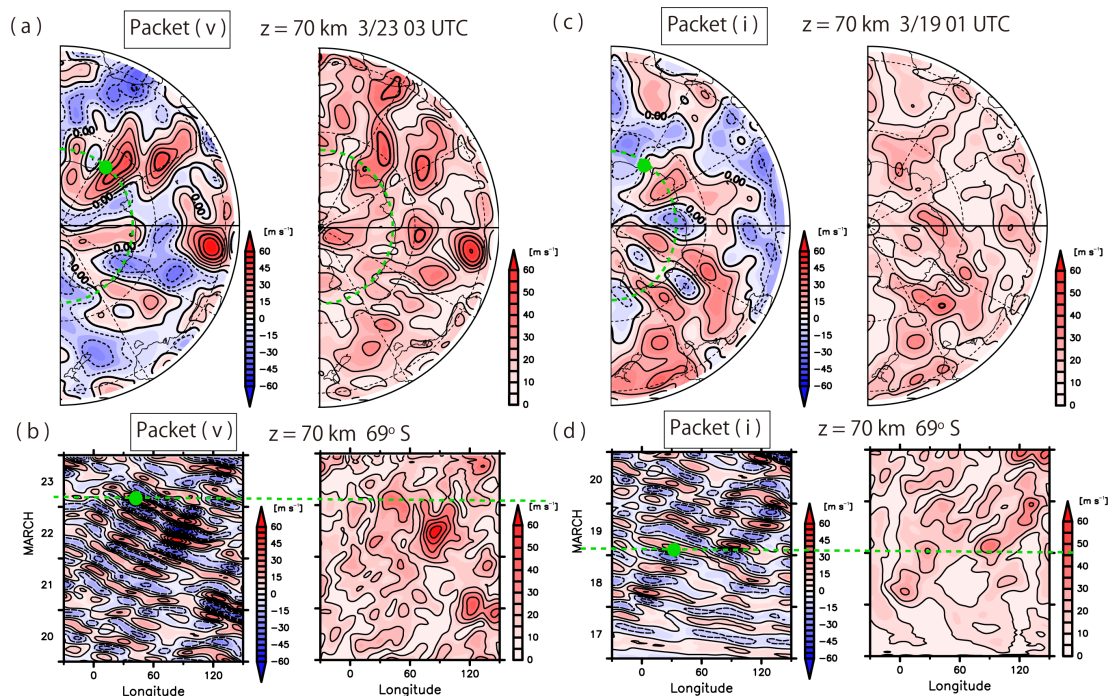
Figure 11. Snapshots of the zonal wind components and their envelope function of the large-scale inertia–gravity waves **(a)** at the height of 70 km at 03:00 UTC, 23 March 2015, corresponding to the packet (v), and **(c)** at the height of 70 km at 01:00 UTC, 19 March 2015, corresponding to the packet (i). Hovmöller diagrams of the zonal wind components and their envelope function of the large-scale inertia–gravity waves at the height of 70 km at 69° S for the period **(b)** from 20 to 23 March and **(d)** from 17 to 20 March. The green dashed curves in **(a)** and **(c)** denote the cross section taken in **(b)** and **(d)**, and vice versa. The green circles are locations of traced wave packets by the method discussed in the text. The contour intervals are 10 m s⁻¹. The data are from the NICAM simulation.

Table 3. The results of the manual wave packet tracing and the ray tracing.

		Manual wave packet tracing			Ray tracing		
		Longitude (° E)	Latitude (° S)	Altitude (km)	Longitude (° E)	Latitude (° S)	Altitude (km)
Packet (v)	3/23 03 UTC	40	67	70.0	40.0	67.0	70.0
	3/22 23 UTC	68	66	60.0	46.2	65.6	63.9
	3/22 16 UTC	75	62	50.0	58.0	62.0	46.8
	3/22 08 UTC	63	52	40.0	71.5	57.2	33.1
	3/22 03 UTC	84	53	30.0	80.8	55.4	27.0
	3/21 16 UTC	80	43	25.0	103.3	51.1	10.3
	3/21 03 UTC	95	41	23.0	–	–	–
Packet (i)	3/19 01 UTC	30	70	70.0	30.0	70.0	70.0
	3/18 19 UTC	32	67	63.0	39.7	68.5	63.1
	3/18 15 UTC	33	66	58.0	47.0	66.7	56.3
	3/18 11 UTC	30	62	53.0	53.5	63.7	49.7
	3/18 08 UTC	30	59	48.0	57.7	61.0	44.6

waves, we apply a low-pass filter in the zonal and meridional directions with a cutoff length of 1000 km in advance. Figure 15 shows horizontal maps of the absolute value of the horizontal wind and ∆NBE at a height of 10 km for 03:00 UTC on 21 March. The absolute value of the horizontal wind is also denoted by thick contours. It is clear that large values are observed in ∆NBE around the tropospheric

jet meandering around (110° E, 40° S), where packet (v) was located. This feature suggests not only that the imbalance in the tropospheric jet was significant but also that packet (v) may have been generated by the spontaneous radiation mechanism.

Next, we examined a possible generation mechanism for packet (i). The disappearance of the clear wave structure at
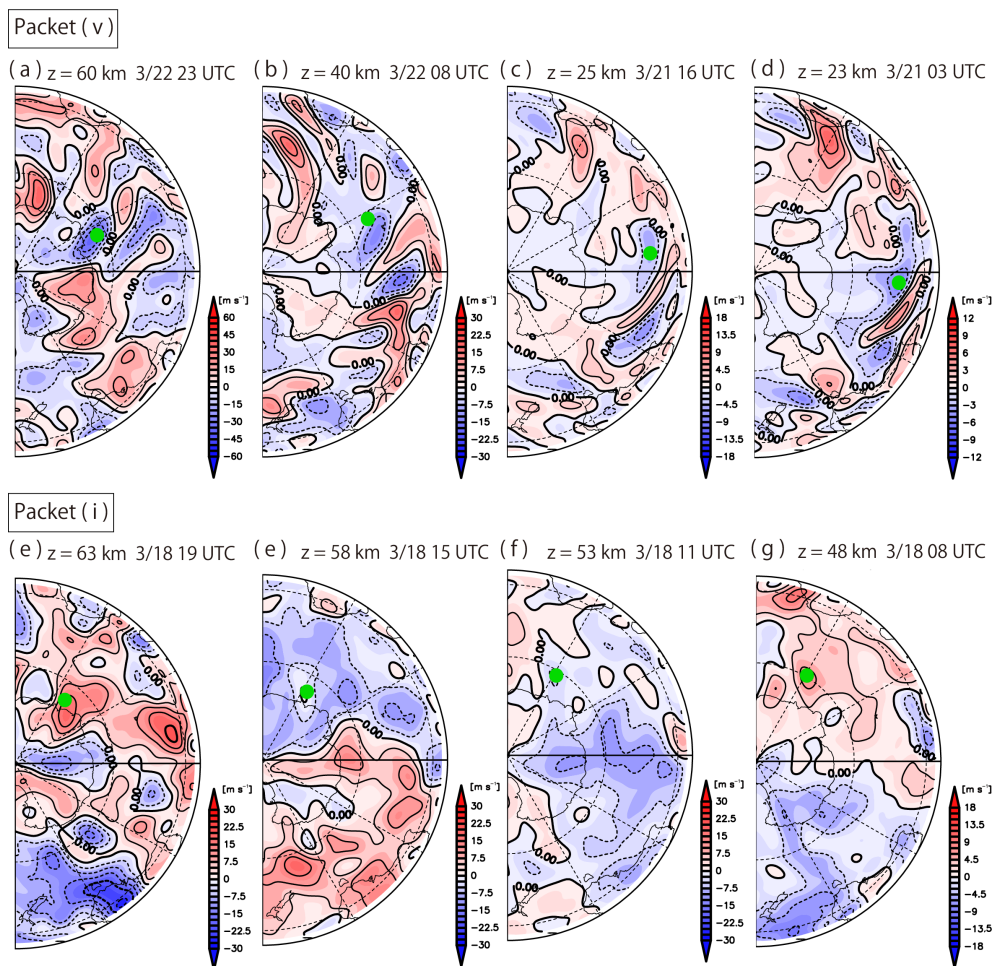
Figure 12. Snapshots of the zonal wind components of the large-scale inertia–gravity waves tracing the packet (v) **(a)** at the height of 60 km at 23:00 UTC, 22 March (contour interval $10 \, \mathrm{m \, s^{-1}}$), **(b)** at the height of 40 km at 08:00 UTC, 22 March (contour interval $5 \, \mathrm{m \, s^{-1}}$), **(c)** at the height of 25 km at 16:00 UTC, 21 March (contour interval $3 \, \mathrm{m \, s^{-1}}$), and **(d)** at the height of 23 km at 03:00 UTC, 21 March (contour interval $2 \, \mathrm{m \, s^{-1}}$). Snapshots for the packet (i) **(e)** at the height of 63 km at 23:00 UTC, 22 March, **(f)** at the height of 58 km at 15:00 UTC, 18 March, **(g)** at the height of 53 km at 11:00 UTC, 18 March (contour interval $5 \, \mathrm{m \, s^{-1}}$), and **(d)** at the height of 48 km at 08:00 UTC, 18 March (contour interval $3 \, \mathrm{m \, s^{-1}}$). The green circles are locations of traced wave packets by the method discussed in the text. The data are from the NICAM simulation.

a height of 53 km (Fig. 12f and g) may indicate that the source of packet (i) is found at this height. A plausible generation mechanism of inertia–gravity waves in the upper stratosphere is spontaneous radiation from the polar night jet (e.g., Sato and Yoshiki, 2008). It is also worth noting that observational studies show high percentages of downward gravity wave propagation in the polar stratosphere compared to those found at low and middle latitudes (e.g., Yoshiki and Sato, 2000; Guest et al., 2000; Moffat-Griffin et al., 2013; Murphy et al., 2014; Mihalikova et al., 2016). To confirm this possibility, we examined fluctuation characteristics and background zonal winds of the upper stratosphere. Figure 16 shows a longitude–height cross section of fluctuation components ($\sqrt{\rho_0 u'}$) and the background zonal wind at 15:00 UTC on 18 March at 65° S. The background zonal wind is ob-
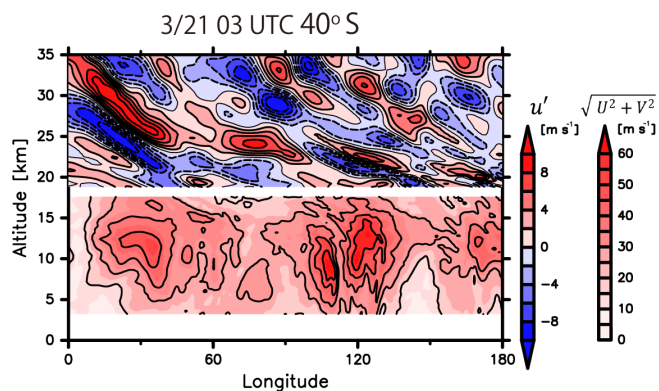
tained using a low-pass filter with a cutoff zonal wavelength of approximately 5000 km.

Interestingly, it seems that fluctuations show symmetric features above and below the core of the polar night jet at a height of 50 km. The height at which packet (i) becomes obscured roughly corresponds to the core of the polar night jet (Fig. 12f and g). These results imply that fluctuations are generated at a height close to the core of the polar night jet. To confirm this, we examined the vertical profile of the energy flux $\overline{p'w'}$ (Fig. 16b). The average was calculated for the longitudinal region spanning from −90 to 60° E. The energy flux is upward above and downward below the core of the polar night jet. This result supports the hypothesis that packet (i) was generated at a height close to the core of the polar night jet.
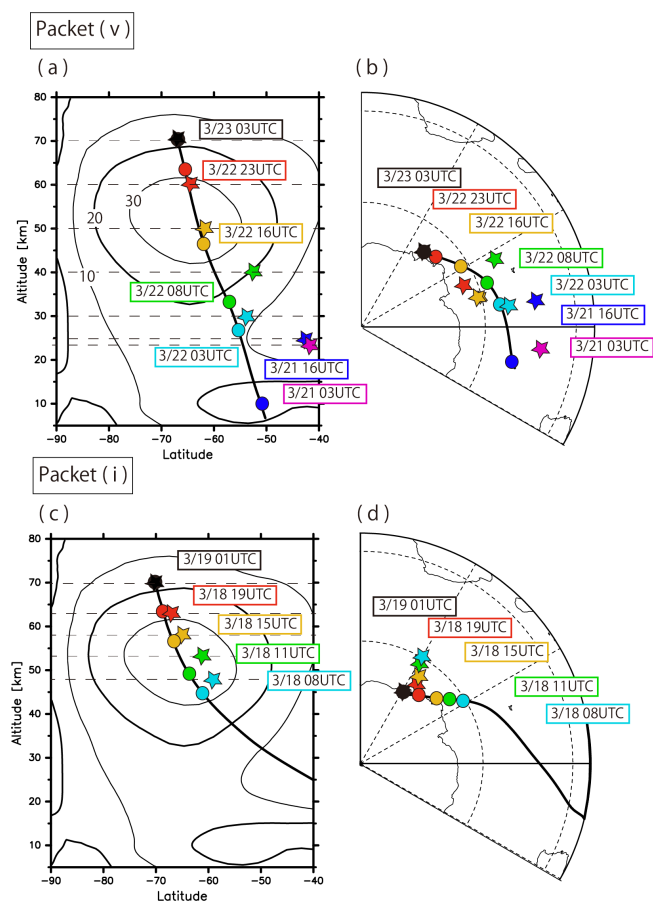
Figure 13. The ray path of **(a, b)** the packet (v) simulated by NICAM and **(c, d)** the packet (i) using the idealized ray tracing method (black thick line, colored circles) and the manual wave packet tracing method (colored star marks) in **(a, c)** the latitude–height cross section and **(b, d)** the horizontal map. The contours in **(a, c)** denote background zonal wind components averaged in the zonal direction and for the period from 17 to 23 March.
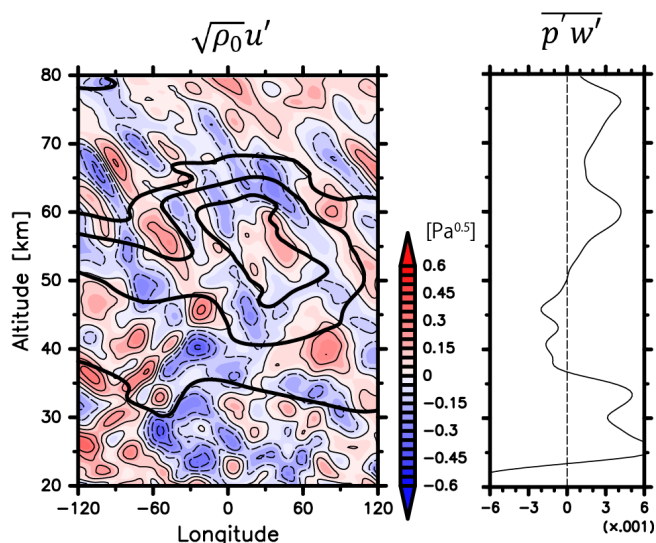
Figure 14. Snapshots of longitude–height cross sections of zonal wind components of the large-scale inertia–gravity waves (above the height of 19 km, the left color bar, contour interval $2\,\mathrm{m\,s^{-1}}$) and the absolute values of the horizontal wind components (below the height of 18 km, the right color bar, contour interval $10\,\mathrm{m\,s^{-1}}$) at 03:00 UTC, 21 March, at $40°$ S. The data are from the NICAM simulation.
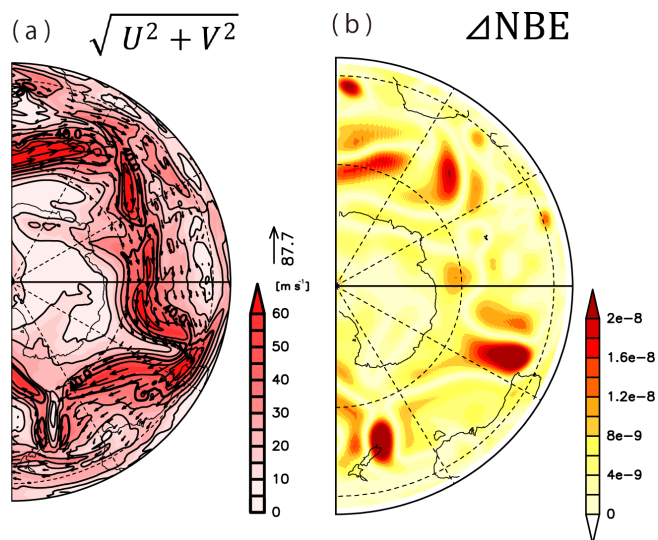
Figure 15. Snapshots of horizontal maps of **(a)** the absolute horizontal wind velocity and **(b)** the residual of the nonlinear balance equation (ΔNBE) at the height of 10 km at 03:00 UTC, 21 March 2015. The vectors in **(a)** denote the directions and the magnitude of the horizontal winds. The contour intervals in **(a)** are $10\,\mathrm{m\,s^{-1}}$. The data are from the NICAM simulation.

This symmetric phase structure observed in Fig. 16a is similar to the structures from the theoretical studies of spontaneous radiation of inertia–gravity waves from a balanced flow (e.g., Yasuda et al., 2015b, their Fig. 6). Yasuda et al. (2015a, b) proposed that the quasi-resonance of gravity waves and a secondary circulation slaved to a balanced jet flow serves as the spontaneous radiation mechanism. The study showed that the quasi-resonance occurs when ground-based wave periods of radiated gravity waves are comparable to the timescale of the slaved motion due to a significant Doppler shift by the strong and balanced flow. Moreover, a timescale in which a fluid particle travels over a descent–ascent couplet structure (i.e., half of an intrinsic period of a radiated gravity wave; $\hat{\tau}$) needs to be shorter than half of the inertial period. This corresponds to the condition that the Lagrangian Rossby number (R_{Lagr}) is greater than unity, which was discussed in McIntyre (2009). Spontaneously radiating

inertia–gravity waves have a shorter wavelength leeward of the jet streak through the wave-capture mechanism (Bühler and McIntyre, 2005). Yasuda et al. (2015a, b) also showed that the source term formula of radiated gravity waves by the quasi-resonance is equal to ΔNBE. However, a large ΔNBE was not observed in the upper stratosphere and mesosphere for the case examined in the present study. The polar night jet around an approximate height of 55 km did not have the strength and/or did not meander enough to cause a large

Figure 16. (a) A longitude–height cross section of zonal wind components of the large-scale inertia–gravity waves $\sqrt{\rho_0}u'$ at 65° S at 15:00 UTC, 18 March (contour interval 0.1 Pa$^{0.5}$), and **(b)** a line plot of the energy flux $\overline{p'w'}$ averaged from the longitude of −90° E to the longitude of 60° E denoted by black arrows. The thick black contours show background zonal wind components extracted by a low-pass filter with a cutoff wavelength of 4000 km. The thick contours denote 20, 30 and 40 m s^{-1}, respectively. The data are from the NICAM simulation.

ΔNBE (not shown). Thus, a different mechanism needs to be considered to explain the spontaneous radiation of gravity waves in the upper stratosphere and mesosphere.

Taking into account the fact that the time variation of the westerly jet around 55 km is mainly caused by migrating tides, we propose a new mechanism for the spontaneous radiation in the upper stratosphere and mesosphere. Figure 17 shows the schematic illustration. Figure 17a shows anomalies of θ from the zonal mean and vertical wind couplets associated with a semidiurnal migrating tide at the height of the core of the polar night jet in the longitudinal direction. As vertical winds are adiabatically present along the modulated θ surface, a mountain-wave-like generation that was discussed in the previous studies may occur. In this case, the vertical winds oscillate with a period of 12 h due to the time variation of the θ surface associated with the semidiurnal migrating tide. The deformation of the θ surface is not caused by the slaved components of the large-scale balanced flow, and hence ΔNBE is not necessarily large. An intrinsic period $\hat{\tau}$ for this case is calculated as $\hat{\tau} = L/(U + U_{\text{tide}})$, where L is a half-length of the latitude circle, U is a speed of the zonal wind and U_{tide} is a ground-based phase speed of the semidiurnal tide. Since L/U_{tide} is 12 h, $\hat{\tau}$ is less than a half of the inertial period in the westerly background wind ($U > 0$). Therefore, gravity waves with a period of 12 h are likely radiated around the jet core. In addition, because of the horizontal shear of the background wind, including the migrat-

ing tides, the wave capture can occur to cause the horizontal wavelength of the radiated gravity waves to be less than that of the semidiurnal migrating tide, which was observed.

Next, we confirm whether the patterns of θ anomalies and vertical velocities associated with the migrating tides are seen in the simulation data. Figure 18a shows the Hovmöller diagram of θ anomalies and vertical velocities associated with the diurnal and semidiurnal migrating tides at a height of 55 km at 65° S. The phase relation of θ and vertical velocities are adiabatic, which is consistent with the scenario shown in Fig. 17a. The θ anomalies associated with the semidiurnal tide seem modulated and partly amplified by the presence of the diurnal migrating tide. Figure 18b shows the Hovmöller diagram of θ and vertical winds of the large-scale gravity wave components, overlaid by the background zonal wind. Note that the background zonal wind is largely modulated by the migrating tides. It is interesting that packet (i) seems to be generated near 30° E at about 12:00 UTC when the packet is located downstream of the zonal wind maxima, which is consistent with the source location and generation timing estimated by the manual packet tracing method. This fact suggests that the wave-capture mechanism is acting in association with the migrating tides. This is the most likely mechanism of packet (i) generation.

We also examined sources of other wave packets (ii), (iii) and (iv) and of other wave packets that are dominant at different longitudes (Fig. 9). The results suggest that these wave packets were also generated by spontaneous radiation from the upper-tropospheric jet stream or from the polar night jet stream (not shown in detail).

5 Discussion

As is shown in Sect. 4, wave structures with large amplitudes in the lower mesosphere (below 80 km) with the ground-based period of quasi-12 h are likely attributable to large-scale inertia–gravity waves. The horizontal wavelengths of quasi-12 h inertia–gravity waves range from 1500 to 2500 km, as shown in Table 2. This conclusion diverges from suggestions made in previous studies, which posit that 12 h disturbances can be either migrating semidiurnal tides of zonal wavenumber two or non-migrating semidiurnal tides of zonal wavenumber one. This difference can be attributed to the difference in observed height regions as follows: height regions examined in this study include the upper stratosphere and lower mesosphere below 80 km while those examined in previous studies include the mesosphere located above 85 km.
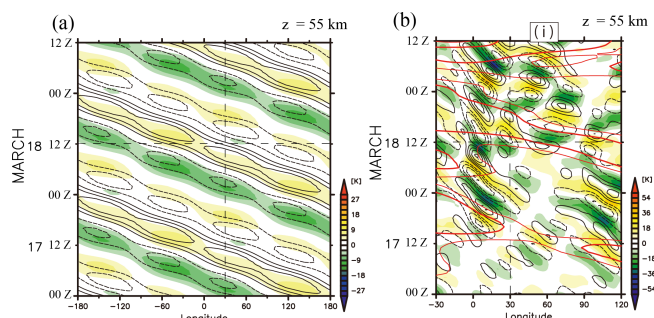
Large-scale inertia–gravity waves with horizontal wavelengths of longer than 1000 km in the mesosphere have already been reported in several studies (Li et al., 2007; Lu et al., 2009, Nicolls et al., 2010; Chen et al., 2013). For example, Nicolls et al. (2010), using the Poker Flat Incoherent Scatter Radar system, found large-amplitude coherent wave
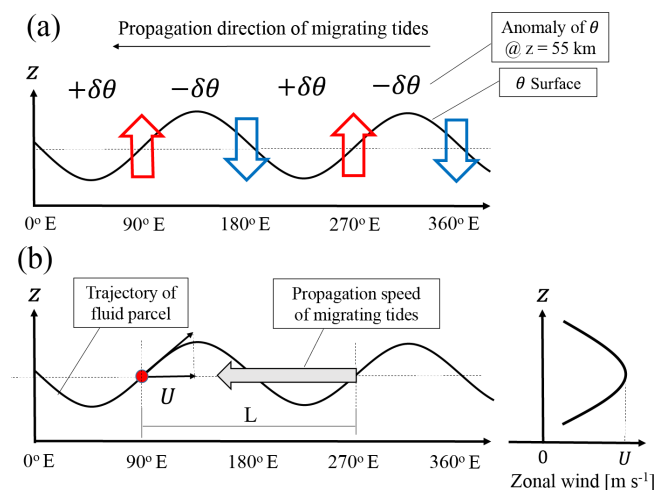
Figure 17. (a) A schematic figure of longitudinal locations of anomalies of θ ($\delta\theta$) from the zonal mean due to the semidiurnal tide and associated vertical wind couplets denoted by large arrows at a height of the core of the polar night jet. **(b)** A trajectory of fluid parcel on a θ surface at the height of polar night jet. The thin dashed arrow denotes a motion of the fluid parcel, and U denotes the magnitude of the background zonal wind.

Figure 18. (a) A Hovmöller diagram of potential temperature (shade) and the vertical wind components (contour) due to the diurnal and semidiurnal migrating tides at the height of 55 km at 65° S. The contour interval is $0.5 \times 10^{-2}\,\mathrm{m\,s^{-1}}$. **(b)** A Hovmöller diagram of potential temperature (shade) and the vertical wind components (black contour) of the large-scale inertia gravity waves, and the zonal wind component with $s = 1$ and $s = 2$ at the height of 55 km at 65° S. The black contour interval is $2.0 \times 10^{-2}\,\mathrm{m\,s^{-1}}$, the red thin contour denotes $30\,\mathrm{m\,s^{-1}}$ and the red thick contour denotes $35\,\mathrm{m\,s^{-1}}$. The data are from the NICAM simulation.

packets with wave periods of roughly 10.5 h and horizontal wavelengths of 700 to 1600 km in the mesosphere. Nicolls et al. (2010) cited jet stream adjustment in the tropopause as a potential source. Chen et al. (2013) also estimated a source for one inertia–gravity wave with a horizontal wavelength of 2200 km, a period of 7.7 h and a vertical wavelength of 22 km, which was observed in the Antarctic mesopause region by combined Fe lidar–MF radar measurements. They heuristically traced the inertia–gravity wave back to a region of unbalanced flow in the stratosphere ($z \sim 43$–46 km). However, no previous studies have directly examined sources of these large-scale inertia–gravity waves in the mesosphere using a numerical model. This study examines the propagation of such large-scale inertia–gravity waves and generation by spontaneous radiation from the polar night jet and tropospheric jet, combining the observational data and numerical simulation outputs.

Recently, Sato et al. (2017) showed that zonal (meridional) momentum flux spectra at the summer mesosphere over Syowa Station are mainly positive (negative), and an isolated peak of the momentum fluxes is observed near a frequency of 12 h, using continuous observations of polar mesosphere summer echoes at heights from 81 to 93 km by the PANSY radar. The signs of momentum flux suggest that gravity waves propagate from low-latitude regions on the assumption of upward propagation. Yasui et al. (2016) also suggested that gravity waves in the summer mesosphere may originate from the tropical convections using the MF radar observation at Syowa Station. Sato et al. (1999) indicated that such meridional propagation of the inertia–gravity

waves from the low-latitude region and the critical-level filtering mechanism can explain the isolated energy peak near the inertia frequency (near a frequency of 12 h at Syowa Station). Moreover, the tide-induced spontaneous radiation mechanism proposed in this study implies frequent generations of quasi-12 h inertia–gravity waves at the polar vortex. Further studies are needed to clarify physical mechanisms for the existence of the isolated energy peak near 12 h in the mesosphere at Syowa Station.

We have further examined vertical fluxes of zonal and meridional momentum associated with large-scale inertia–gravity waves $\rho_0\overline{u'w'}$ and $\rho_0\overline{v'w'}$. The overbar denotes a zonal averaging operation. Figure 19a and b show latitude–height sections of $\rho_0\overline{u'w'}$ and $\rho_0\overline{v'w'}$, respectively, which are averaged for 19 to March 2015. Large negative $\rho_0\overline{u'w'}$ and $\rho_0\overline{v'w'}$ values are distributed approximately 40° S in the lower stratosphere and approximately 75° S in the mesosphere. The signs of $\rho_0\overline{u'w'}$ and $\rho_0\overline{v'w'}$ are consistent with parameter estimations from PANSY radar observations and from the numerical simulation. The slanted structures seem quite similar to the propagation path of packet (v) discussed in Sect. 4.2. Such a slanted structure is likely formed from the meridional propagation of inertia–gravity waves, which is numerically shown and theoretically discussed by Sato et al. (2009, 2012) in terms of refraction and advection by background wind.

Interestingly, Fig. 19a shows that the value of $\rho_0\overline{u'w'}$ is lower in the middle stratosphere, thus showing a peak of negative $\rho_0\overline{u'w'}$ in the mesosphere. Small-scale gravity waves do not follow such a pattern (not shown). This result suggests that parts of large-scale inertia–gravity waves are generated in the upper stratosphere as discussed in Sect. 4.2. In contrast, such a feature is not observed in $\rho_0\overline{v'w'}$, although a small
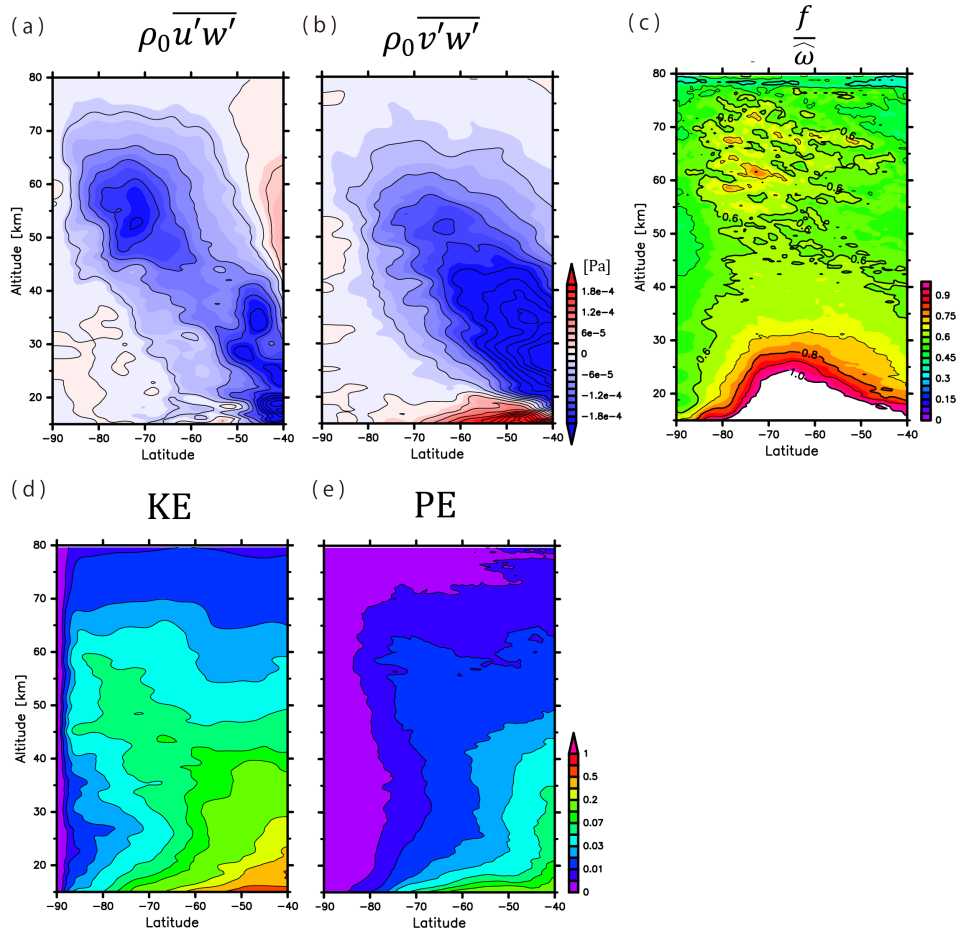
Figure 19. Latitude–height cross sections of **(a)** the vertical fluxes of zonal momentum $\rho_0 \overline{u'w'}$, **(b)** the vertical fluxes of zonal momentum $\rho_0 \overline{v'w'}$, **(c)** the ratio of the Coriolis parameter to the intrinsic frequency $f/\hat{\omega}$, **(d)** the kinetic energies of the horizontal wind components and **(e)** the potential energies of the large-scale inertia–gravity waves, which are averaged in the zonal direction and for the period from 19 to 21 March 2015. The contour interval is **(a, b)** 4.0×10^{-5} [Pa] and **(c)** 0.1, respectively. It should be noted that the color bar and the contour interval in **(d)** and **(e)** are log-scaled. The data are from the NICAM simulation.

negative local maximum is present at heights of 50 to 55 km at approximately 60° S. This result implies that wavenumber vectors of inertia–gravity waves in the mesosphere tend to move eastward, consistent with the parameter estimation shown in Sect. 4.1.

Next, we examined the energy density of the large-scale inertia–gravity waves by dividing the total energy density into the following three components: horizontal wind kinetic energy ($\overline{\mathrm{KE}}$), vertical wind kinetic energy ($\overline{\mathrm{VE}}$) and potential energy ($\overline{\mathrm{PE}}$):

$$\overline{\mathrm{KE}} = \frac{1}{2}\rho_0\left(\overline{u'^2} + \overline{v'^2}\right), \tag{8}$$

$$\overline{\mathrm{VE}} = \frac{1}{2}\rho_0\overline{w'^2}, \tag{9}$$

and

$$\overline{\mathrm{PE}} = \frac{1}{2}\rho_0\frac{g^2}{N^2}\overline{\left(\frac{T'}{T}\right)^2}. \tag{10}$$

According to the linear theory of hydrostatic inertia–gravity waves, the ratio of $\overline{\mathrm{VE}}$ to $\overline{\mathrm{PE}}$ has the following relation (from the thermodynamic equation) (e.g., Wang et al., 2005; Geller and Gong 2010; Geller et al., 2013):

$$\frac{\overline{\mathrm{VE}}}{\overline{\mathrm{PE}}} = \frac{\hat{\omega}^2}{N^2}. \tag{11}$$

Thus, $\left| f / \hat{\omega} \right|$ can be derived as follows:

$$\left|\frac{f}{\hat{\omega}}\right| = \left|\frac{f}{N}\right|\sqrt{\frac{\overline{\mathrm{PE}}}{\overline{\mathrm{VE}}}}. \tag{12}$$

Figure 19c shows the latitude–height section of $\left| f / \hat{\omega} \right|$. In the mesosphere, $\left| f / \hat{\omega} \right|$ ranges from 0.6 to 0.8 at approximately 70° S, which agrees quite well with estimates

from the hodograph analysis (Tables 1 and 2). The fact that $|f / \hat{\omega}|$ has higher values than 0.6 indicates that the large-scale inertia–gravity waves are almost hydrostatic. Note that the value of $|f / \hat{\omega}|$ is larger than 1.0 in the lower stratosphere, which is inconsistent with the linear theory of inertia–gravity waves. This implies that the large-scale inertia–gravity waves defined in Sect. 4.1 include balanced components in the lower stratosphere (e.g., baroclinic wave components) as well as large-scale inertia–gravity waves.

Figure 19d and e show latitude–height sections of $\overline{KE}$ and $\overline{PE}$ for the large-scale inertia–gravity waves. The slanted structures in Fig. 19a and b are also shown in Fig. 19d and e. It should be noted that the ratio of the Coriolis parameter to the intrinsic frequency $(f / \hat{\omega})$ can also be obtained from $\overline{KE}$ and $\overline{PE}$ as follows:

$$\left| \frac{f}{\hat{\omega}} \right| = \sqrt{\frac{\frac{\overline{KE}}{\overline{PE}} - 1.}{\frac{\overline{KE}}{\overline{PE}} + 1}}. \tag{13}$$

We confirmed that $(f / \hat{\omega})$ values obtained by Eq. (13) are consistent with the result obtained from Eq. (12) (not shown).

6 Summary

The first observation with a complete system of the PANSY radar were successfully performed for 16–24 March 2015. During this period, quasi-12 h disturbances in the mesosphere at heights of 70 to 80 km were detected by the PANSY radar system. Our main results are summarized as follows.

The observed wave period and vertical wavelength are about 12.3 h and 13.8 km, respectively. The estimated horizontal wavelength is longer than 1100 km. The wavenumber vectors tend to be directed northeastward or southwestward. Ratios of the Coriolis parameter to the intrinsic frequency range from 0.6 to 0.85.

Moreover, using the nonhydrostatic numerical model with a model top of 87 km, we succeeded in simulating quasi-12 h disturbances in the mesosphere. Using time and spatial filters, we found that quasi-12 h disturbances are attributable not to semidiurnal migrating tides but rather to large-scale inertia–gravity waves with horizontal wavelengths of longer than 1400 km. Wavenumber vectors simulated in the NICAM are directed northeastward. Wave parameters directly estimated using the NICAM agree quite well with those estimated by the PANSY radar observation system.

The detected inertia–gravity waves were likely generated by the spontaneous radiation mechanism of the midlatitude upper-tropospheric jet at the tropopause or the polar night jet. Inertia–gravity waves generated near the midlatitude tropopause propagate laterally and vertically to the polar mesosphere.

A new spontaneous radiation mechanism associated with the semidiurnal migrating tides is proposed. This mechanism explains a radiation of inertia–gravity wave with a period of 12 h in the upper stratosphere and mesosphere. The wave-capture mechanism is important downstream of a zonal wind maxima caused by the migrating tides.

Vertical fluxes of the zonal and meridional momentum of large-scale inertia–gravity waves show a slanted structure from the midlatitude lower stratosphere to the polar mesosphere. Moreover, the vertical flux of the zonal momentum shows a strong negative peak in the mesosphere, suggesting the generation of large-scale inertia–gravity waves in the upper stratosphere.

The present study offers a quantitative discussion based on high-resolution observations and numerical models. Statistical analyses of large-scale inertia–gravity waves in the real atmosphere will be of interest for future studies using observations and numerical simulations in the different seasons.

References

Akmaev, R. A., Forbes, J. M., Lübken, F.-J., Murphy, D. J., and Höffner, J.: Tides in the mesopause region over Antarctica: Comparison of whole atmosphere model simulations with ground-based observations, J. Geophys. Res.-Atmos., 121, 1156–1169, doi:10.1002/2015JD023673, 2016.

Alexander, M. J., Geller, M., McLandress, C., Polavarapu, S., Preusse, P., Sassi, F., Sato, K., Eckermann, S., Ern, M., Hertzog, A., Kawatani, Y., Pulido, M., Shaw, T., Sigmond, M., Vincent, R., and Watanabe, S.: Recent developments in gravity wave effects in climate models, and the global distribution of gravity wave momentum flux from observations and models, Q. J. Roy. Meteor. Soc., 136, 1103–1124, 2010.

Aso, T.: A note on the semidiurnal non-migrating tide at polar latitudes, Earth Planets Space, 59, e21–e24, 2007.

Baldwin, M. P., Gray, L. J., Dunkerton, T. J., Hamilton, K., Haynes, P. H., Randel, W. J., Holton, J. R., Alexander, M. J., Hirota, I., Horinouchi, T., Jones, D. B. A., Kinnersley, J. S., Marquardt, C., Sato, K., and Takahashi, M.: The Quasi-Biennial Oscillation, Rev. Geophys., 39, 179–229, doi:10.1029/1999RG000073, 2003.

Becker, E.: Sensitivity of the upper mesosphere to the Lorenz energy cycle of the troposphere, J. Atmos. Sci., 66, 647–666, doi:10.1175/2008JAS2735.1, 2009.

Bloom, S., Takacs, L., DaSilva, A., and Ledvina, D.: Data assimilation using incremental analysis updates, Mon. Weather Rev., 124, 1256–1271, 1996.

Bühler, O. and McIntyre, M. E.: Wave capture and wave-vortex duality, J. Fluid. Mech., 534, 67–95, 2005.

Chen, C., Chu, X., McDonald, A. J., Vadas, S. L., Yu, Z., Fong, W., and Lu, X.: Inertia-gravity waves in Antarctica: A case study using simultaneous lidar and radar measurements at McMurdo/Scott Base (77.8° S, 166.7° E), J. Geophys. Res.-Atmos., 118, 2794–2808, 2013.

Cherniak, I. and Zakharenkova, I.: High-latitude ionospheric irregularities: differences between ground- and space-based GPS measurements during the 2015 St. Patrick's Day Storm, Earth Planets Space, 68, 136, doi:10.1186/s40623-016-0506-1, 2016.

Chu, X., Huang, W., Fong, F., Yu, Z., Wang, Z., Smith, J. A., and Gardner, C. S.: First lidar observations of polar mesospheric clouds and Fe temperatures at McMurdo (77.8° S, 166.7° E), Antarctica, Geophys. Res. Lett., 38, L16810, doi:10.1029/2011GL048373, 2011.

Collins, R. L., Senft, D. C., and Gardner, C. S.: Observations of a 12 H wave in the mesopause region at the South Pole, Geophys. Res. Lett., 19, 57–60, doi:10.1029/91GL02780, 1992.

Eyring, V., Shepherd, T. G., and Waugh, D. W. (Eds.): SPARC CCMVal report on the evaluation of chemistry-climate models. SPARC Rep. 5, WCRP-132, WMO/TD-No. 1526, 434 pp., 2010.

Fisher, G. M., Niciejewski, R. J., Killeen, T. L., Gault, W. A., Shepherd, G. G., Brown, S., and Wu, Q.: Twelve-hour tides in the winter northern polar mesosphere and lower thermosphere, J. Geophys. Res.-Space, 107, 1211, doi:10.1029/2001JA000294, 2002.

Forbes, J. M., Makarov, N. A., and Portnyagin, Y. I.: First results from the meteor radar at south pole: A large 12-hour oscillation with zonal wavenumber one, Geophys. Res. Lett., 22, 3247–3250, 1995.

Forbes, J. M., Portnyagin, Y. I., Markov, N. A., Palo, S. E., Merzlyakov, E. G., and Zhang, X.: Dynamics of the lower thermosphere over South Pole from meteor radar windmeasurements, Earth Planets Space, 51, 611–620, 1999.

Fraser, G. J. and Khan, U.: Semidiurnal variations in the time scale of irregularities near the Antarctic summer mesopause, Radio Science, 25, 997–1003, 1990.

Fritts, D. C. and Alexander, M. J.: Gravity wave dynamics and effects in the middle atmosphere, Rev. Geophys., 41, 1003, doi:10.1029/2001RG000106, 2003.

Fritts, D. C., Riggin, D. M., Balsley, B. B., and Stockwell, R. G.: Recent results with an MF radar at McMurdo, Antarctica: Characteristics and variability of motions near 12-hour period in the mesosphere, Geophys. Res. Lett., 25, 297–300, doi:10.1029/97GL03702, 1998.

Geller, M. A. and Gong, J.: Gravity wave kinetic, potential, and vertical fluctuation energies as indicators of different frequency gravity waves, J. Geophys. Res.-Atmos., 115, D11111, doi:10.1029/2009JD012266, 2010.

Geller, M. A., Alexander, M., Love, P. T., Bacmeister, J., Ern, M., Hertzog, A., and Zhou, T.: A Comparison between Gravity Wave Momentum Fluxes in Observations and Climate Models, J. Climate, 26, 6383–6405, doi:10.1175/JCLI-D-12-00545.1, 2013.

Guest, F. M., Reeder, M. J., Marks, C. J., and Karoly, D. J.: Inertia-gravity waves observed in the lower stratosphere over Macquarie Island, J. Atmos. Sci., 57, 737–752, 2000.

Hagan, M. E. and Forbes, J. M.: Migrating and nonmigrating semidiurnal tides in the upper atmosphere excited by tropospheric latent heat release, J. Geophys. Res., 108, 1062, doi:10.1029/2002JA009466, 2003.

Haynes, P. H.: The latitudinal structure of the quasi-biennial oscillation, Q. J. Roy. Meteor. Soc., 124, 2645–2670, 1998.

Hernandez, G., Fraser, G. J., and Smith, R. W.: Mesospheric 12-hour oscillation near South Pole, Antarctica, Geophys. Res. Lett., 20, 1787–1790, doi:10.1029/93GL01983, 1993.

Hertzog, A., Boccara, G., Vincent, R. A., Vial, F., and Cocquerez, P.: Estimation of gravity wave momentum flux and phase speeds from quasi-Lagrangian stratospheric balloon flights. Part II: Results from the Vorcore campaign in Antarctica, J. Atmos. Sci., 65, 3056–3070, 2008.

Hirota, I. and Niki, T.: Inertia-gravity waves in the troposphere and stratosphere observed by the MU radar, J. Meteorol. Soc. Jpn., 64, 995–999, 1986.

Jacobsen, K. S. and Andalsvik, Y. L.: Overview of the 2015 St. Patrick's Day storm and its consequences for RTK and PPP positioning in Norway, J. Space Weather Space Clim., 6, A9, doi:10.1051/swsc/2016004, 2016.

Jacobsen, K. S. and Dähnn, M.: Statistics of ionospheric disturbances and their correlation with GNSS 338 positioning errors at high latitudes, J. Space Weather Space Clim., 4, A27, doi:10.1051/swsc/2014024, 2014.

Kataoka, R., Shiota, D., Kilpua, E., and Keika, K.: Pileup accident hypothesis of magnetic storm on 17 March 2015, Geophys. Res. Lett., 42, 5155–5161, doi:10.1002/2015GL064816, 2015.

Kohma, M. and Sato, K.: The effects of atmospheric waves on the amounts of polar stratospheric clouds, Atmos. Chem. Phys., 11, 11535–11552, doi:10.5194/acp-11-11535-2011, 2011.

Lane, T. P., Doyle, J. D., Plougonven, R., Shapiro, M. A., and Sharman, R. D.: Observations and numerical simulations of inertia-gravity waves and shearing instabilities in the vicinity of a jet stream, J. Atmos. Sci., 61, 2792–2706, 2004.

Li, T., She, C.-Y., Liu, H.-L., Leblanc, T., and McDermid, I. S.: Sodium lidar–observed strong inertia-gravity wave activities in the mesopause region over Fort Collins, Colorado (41° N, 105° W), J. Geophys. Res., 112, D22104, doi:10.1029/2007JD008681, 2007.

Liu, H. L., McInerney, J. M., Santos, S., Lauritzen, P. H., Taylor, M. A., and Pedatella, N. M.: Gravity waves simulated by high resolution Whole Atmosphere Community Climate Model, Geophys. Res. Lett., 41, 9106–9112, 2014.

Lu, X., Liu, A. Z., Swenson, G. R., Li, T., Leblanc, T., and McDermid, I. S.: Gravity wave propagation and dissipation from the stratosphere to the lower thermosphere, J. Geophys. Res., 114, D11101, doi:10.1029/2008JD010112, 2009.

Marks, C. J. and Eckermann, S. D.: A three-dimensional nonhydrostatic ray tracing model for gravity waves: Formulation and preliminary results for the middle atmosphere. J. Atmos. Sci., 52, 1959–1984, 1995.

Mayr, H. G., Mengel, J. G., Talaat, E. R., Porter, H. S., and Chan, K. L.: Mesospheric non-migrating tides generated with planetary waves: I. Characteristics, J. Atmos. Sol.-Terr. Phys., 67, 959–980, 2005a.

Mayr, H. G., Mengel, J. G., Talaat, E. R., Porter, H. S., and Chan, K. L.: Mesospheric non-migrating tides generated with planetary waves: II. Influence of gravity waves, J. Atmos. Sol.-Terr. Phys., 67, 981–991, 2005b.

McDonald, A. J., George, S. E., and Woollands, R. M.: Can gravity waves significantly impact PSC occurrence in the Antarctic?, Atmos. Chem. Phys., 9, 8825–8840, doi:10.5194/acp-9-8825-2009, 2009.

McFarlane, N. A.: The effect of orographically excited wave drag on the general circulation of the lower stratosphere and troposphere, J. Atmos. Sci., 44, 1775–1800, 1987.

McIntyre, M. E.: Spontaneous imbalance and hybrid vortex- gravity structures, J. Atmos. Sci., 66, 1315–1326, doi:10.1175/2008JAS2538.1, 2009.

McLandress, C., Shepherd, T. G., Polavarau, S., and Beagley, S. R.: Is Missing Orographic Gravity Wave Drag near 60° S the Cause of the Stratospheric Zonal Wind Biases in Chemistry–Climate Models?, J. Atmos. Sci., 69, 802–818, 2012.

Mihalikova, M., Sato, K., Tsutsumi, M., and Sato, T.: Properties of inertia-gravity waves in the lowermost stratosphere as observed by the PANSY radar over Syowa Station in the Antarctic, Ann. Geophys., 34, 543–555, doi:10.5194/angeo-34-543-2016, 2016.

Moffat-Griffin, T., Jarvis, M. J., Colwell, S. R., Kavanagh, A. J., Manney, G. L., and Daffer, W. H.: Seasonal variations in the lower stratospheric gravity wave energy above the Falkland Islands, J. Geophys. Res.-Atmos., 118, 10861–10869, doi:10.1002/jgrd.50859, 2013.

Murphy, D. J., Forbes, J. M., Walterscheid, R. L., Hagan, M. E., Avery, S. K., Aso, T., Fraser, G. J., Fritts, D. C., Jarvis, M. J., McDonald, A. J., Riggin, D. M., Tsutsumi, M., and Vincent, R. A.: A climatology of tides in the Antarctic mesosphere and lower thermosphere, J. Geophys. Res., 111, D23104, doi:10.1029/2005JD006803, 2006.

Murphy, D. J., Aso, T., Fritts, D. C., Hibbins, R. E., McDonald, A. J., Riggin, D. M., Tsutsumi, M., and Vincent, R. A.: Source regions for Antarctic MLT non-migrating semidiurnal tides, Geophys. Res. Lett., 36, L09805, doi:10.1029/2008GL037064, 2009.

Murphy, D. J., Alexander, S. P., Klekociuk, A. R., Love, P. T., and Vincent, R. A.: Radiosonde observations of gravity waves in the lower stratosphere over Davis, Antarctica, J. Geophys. Res.-Atmos., 119, 11973–11996, doi:10.1002/2014JD022448, 2014.

Nakamura, T., Tsuda, T., Yamamoto, M., Fukao, S., and Kato, S.: Characteristics of gravity waves in the meso-

sphere observed with the middle and upper atmosphere radar 2. Propagation direction, J. Geophys. Res., 98, 8911–8923, doi:10.1029/92JD03030, 1993.

Nakanishi, M. and Niino, H.: An Improved Mellor–Yamada Level-3 Model with Condensation Physics: Its Design and Verification, Bound.-Lay. Meteorol. 112, 1–31, 2004.

Nastrom, G. D. and Eaton, F. D.: Quasi-monochromatic inertiagravity waves in the lower stratosphere from MST radar observations, J. Geophys. Res., 111, D19103, doi:10.1029/2006JD007335, 2006.

Nicolls, M. J., Varney, R. H., Vadas, S. L., Stamus, P. A., Heinselman, C. J., Cosgrove, R. B., and Kelley, M. C.: Influence of an inertia-gravity wave on mesospheric dynamics: A case study with the Poker Flat Incoherent Scatter Radar, J. Geophys. Res., 115, D00N02, doi:10.1029/2010JD014042, 2010.

Okamoto, K., Sato, K., and Akiyoshi, H.: A study on the formation and trend of the Brewer-Dobson circulation, J. Geophys. Res., 116, D10117, doi:10.1029/2010JD014953, 2011.

O'Sullivan, D. J. and Dunkerton, T. J.: Generation of inertia-gravity waves in a simulated life cycle of baroclinic instability, J. Atmos. Sci., 52, 3695–3716, 1995.

Pavelin, E. G., Whiteway, J. A., and Vaughan, G.: Observation of gravity wave generation and breaking in the lowermost stratosphere, 2001: J. Geophys. Res., 106, 5173–5179, 2001.

Plougonven, R. and Snyder, C.: Inertia-gravity waves spontaneously generated by jets and fronts. Part I: Different baroclinic life cycles, J. Atmos. Sci., 64, 2502–2520, 2007.

Plumb, R. A.: Stratospheric transport, J. Meteorol. Soc. Jpn., 80, 793–809, 2002.

Portnyagin, Y. I., Forbes, J. M., Makarov, N. A., Merzlyakov, E. G., and Palo, S.: The summertime 12-h wind oscillation with zonal wavenumber s = 1 in the lower thermosphere over the South Pole, Ann. Geophys., 16, 828–837, doi:10.1007/s00585-998-0828-9, 1998.

Reid, I. M. and Vincent, R. A.: Measurements of mesospheric gravity wave momentum fluxes and mean flow accelerations at Adelaide, Australia, J. Atmos. Terr. Phys., 49, 443–460, 1987.

Richter, J. H., Sassi, F., and Garcia, R. R.: Toward a physically based gravity wave source parameterization in a general circulation model, J. Atmos. Sci., 67, 136–156, 2009.

Rienecker, M., Suarez, M. J., Gelaro, R., Todling, R., Bacmeister, J., Liu, E., Bosilovich, M. G., Schubert, S. D., Takacs, L., Kim, G.-K., Bloom, S., Chen, J., Collins, D., Conaty, A., da Silva, A., Gu, W., Joiner, J., Koster, R. D., Lucchesi, R., Molod, A., Owens, T., Pawson, S., Pegion, P., Redder, C. R., Reichle, R., Robertson, F. R., Ruddick, A. G., Sienkiewicz, M., and Woollen, J.: MERRA: NASA's ModernEra Retrospective Analysis for Research and Applications, J. Climate, 24, 3648–3624, 2011.

Riggin, D. M., Fritts, D. C., Jarvis, M. J., and Jones, G. O. L.: Spatial structure of the 12-hour wave in the Antarctic as observed by radar, Earth Planets Space, 51, 621–628, 1999.

Sato, K.: A statistical study of the structure, saturation and sources of inertio-gravity waves in the lower stratosphere observed with the MU radar, J. Atmos. Terr. Phys., 56, 755–774, 1994.

Sato, K. and Dunkerton, T. J.: Estimates of momentum flux associated with equatorial Kelvin and gravity waves, J. Geophys. Res., 102, 26247–26261, 1997.

Sato, K. and Yamada, M.: Vertical structure of atmospheric gravity waves revealed by the wavelet analysis, J. Geophys. Res.-Atmos., 99, 20623–20631, 1994.

Sato, K. and Yoshiki, M.: Gravity wave generation around the polar vortex in the stratosphere revealed y 3-houly radiosonde observations at Syowa Station, J. Atmos. Sci., 65, 3719–3735, 2008.

Sato, K., O'Sullivan, D. J., and Dunkerton, T. J.: Low-frequency inertia-gravity waves in the stratosphere revealed by three-weak continuous observation with the MU radar, Geophys. Res. Lett., 24, 1739–1742, 1997.

Sato, K., Kumakura, T., and Takahashi, M.: Gravity waves appearing in a high-resolution GCM simulation, J. Atmos. Sci. ,56, 1005–1018, doi:10.1175/1520-0469(1999)056<1005:GWAIAH>2.0.CO;2, 1999.

Sato, K., Watanabe, S., Kawatani, Y., Tomikawa, Y., Miyazaki, K., and Takahashi, M.: On the origins of mesospheric gravity waves, Geophys. Res. Lett., 36, L19801, doi:10.1029/2009GL039908, 2009.

Sato, K., Tateno, S., Watanabe, S., and Kawatani, Y.: Gravity wave characteristics in the Southern Hemisphere revealed by a high-resolution middle-atmosphere general circulation model. J. Atmos. Sci., 69, 1378–1396, doi:10.1175/JAS-D-11-0101.1, 2012.

Sato, K., Kinoshita, T., and Okamoto, K.: A new method to estimate three-dimensional residual mean circulation in the middle atmosphere and its application to gravity-wave resolving general circulation model data, J. Atmos. Sci., 70, 3756–3779, doi:10.1175/JAS-D-12-0352.1, 2013.

Sato, K., Tsutsumi, M., Sato, T., Nakamura, T., Saito, A., Tomikawa, Y., Nishimura, K., Kohma, M., Yamagishi, H., and Yamanouchi, T.: Program of the Antarctic Syowa MST/IS Radar (PANSY), J. Atmos. Sol-Terr. Phys., 118A, 2–15, 2014.

Sato, K., Kohma, M., Tsutsumi, M., and Sato, T.: Frequency spectra and vertical profiles of wind fluctuations in the summer Antarctic mesosphere revealed by MST radar observations, J. Geophys. Res.-Atmos., 122, 3–19, 2017.

Satoh, M., Matsuno, T., Tomita, H., Miura, H., Nasuno, T., and Iga, S.: Nonhydrostatic icosahedral atmospheric model (NICAM) for global cloud resolving simulations, J. Comput. Phys., 227, 3486–3514, doi:10.1016/j.jcp.2007.02.006, 2008.

Satoh, M., Tomita, H., Yashiro, H., Miura, H., Kodama, C., Seiki, T., Noda, A. T., Yamada, Y., Goto, D., Sawada, M., Miyoshi, T., Niwa, Y., Hara, M., Ohno, T., Iga, S., Arakawa, T., Inoue, T., and Kubokawa, H.: The Non-hydrostatic Icosahedral Atmospheric Model: Description and Development. Progress in Earth and Planetary Science, 1, 18, doi:10.1186/s40645-014-0018-1, 2014.

Scinocca, J. F.: An accurate spectral nonorographic gravity wave drag parameterization for general circulation models, J. Atmos. Sci., 60, 667–682, 2003.

Shibata, T., Sato, K., Kobayashi, H., Yabuki, M., and Shiobara, M.: The Antarctic polar stratospheric clouds under the temperature perturbation by nonorogaphic inertia-gravity waves observed by micropulse lidar. J. Geophys. Res., 108, 4105, doi:10.1029/2002JD002713, 2003.

Shibuya, R., Sato, K., Tomikawa, Y., Tsutsumi, M., and Sato, T.: A study of multiple tropopause structures caused by inertia-gravity waves in the Antarctica, J. Atmos. Sci., 72, 2109–2130, 2015.

Shibuya, R., Miura, H., and Sato, K.: A grid transformation method for a quasi-uniform, circular fine region using

the spring dynamic, J. Meteorol. Soc. Jpn., 94, 443–452, doi:10.2151/jmsj.2016-022, 2016.

Stolarski, R. S., Douglass, A. R., Gupta, M., Newman, P. A., Pawson, S., Schoeberl, M. R., and Nielsen, J. E.: An ozone increase in the Antarctic summer stratosphere: A dynamical response to the ozone hole, Geophys. Res. Lett., 33, L21805, doi:10.1029/2006GL026820, 2006.

Talaat, E. R. and Mayr, H. G.: Model of semidiurnal pseudo tide in the high-latitude upper mesosphere, J. Atmos. Sol-Terr. Phys., 73, 2386–2391, 2011.

Tomita, H., Satoh, M., and Goto, K.: An optimization of icosahedral grid by using spring dynamics, J. Comp. Phys., 183, 307–331, 2002.

Vaughan, G. and Worthington, R. M.: Inertia-gravity waves observed by the UK MST radar, Q. J. Roy. Meteor. Soc., 133, 179–188, 2007.

Vincent, R. A. and Reid, I. M.: HF Doppler Measurements of Mesospheric Gravity Wave Momentum Fluxes, J. Atmos. Sci., 40, 1321–1333, doi:10.1175/1520-0469(1983)040<1321:HDMOMG> 2.0.CO;2, 1983.

Walterscheid, R. L., Sivjee, G. G., Schubert, G., and Hamwey, R. M.: Large-amplitude semidiurnal temperature variations in the polar mesopause: evidence of a pseudotide, Nature, 324, 347–349, 1986.

Wang, L., Geller, M. A., and Alexander, M. J.: Spatial and temporal variations of gravity wave parameters. Part I: Intrinsic frequency, wavelength, and vertical propagation direction, J. Climate, 62, 125–142, 2005.

Watanabe, S., Sato, K., and Takahashi, M.: A general circulation model study of the orographic gravity waves over Antarctica excited by katabatic winds, J. Geophys. Res., 111, D18104, doi:10.1029/2005JD006851, 2006.

Watanabe, S., Kawatani, Y., Tomikawa, Y., Miyazaki, K., Takahashi, M., and Sato, K.: General Aspects of a T213L256 Middle Atmosphere General Circulation Model, J. Geophys. Res., 113, D12110, doi:10.1029/2008JD010026, 2008.

Watanabe, S., Sato, K., Kawatani, Y., and Takahashi, M.: Vertical resolution dependence of gravity wave momentum flux simulated by an atmospheric general circulation model, Geosci. Model Dev., 8, 1637–1644, doi:10.5194/gmd-8-1637-2015, 2015.

Wu, Q., Killeen, T. L., Nozawa, S., McEwen, D., Guo, W., amd Solomon, S. C.: Observations of mesospheric neutral wind 12-hour wave in the Northern Polar Cap, J. Atmos. Sol.-Terr. Phys., 65, 971–978, 2003.

Wu, W.-S., Purser, R. J., and Parrish, D. F.: Three-dimensional variational analysis with spatially inhomogeneous covariances, Mon. Weather Rev., 130, 2905–2916, 2002.

Yamashita, K., Miyahara, S., Miyoshi, Y., Kawano, K., and Ninomiya, J.: Seasonal variation of non-migrating semidiurnal tide in the polar MLT region in a general circulation model, J. Atmos. Solar-Terr. Phys., 64, 1083–1094, 2002.

Yasuda, Y., Sato, K., and Sugimoto, N.: A Theoretical Study on the Spontaneous Radiation of Inertia-gravity Waves Using the Renormalization Group Method. Part I: Derivation of the Renormalization Group Equations, J. Atmos. Sci., 72, 957–983, doi:10.1175/JAS-D-13-0370.1, 2015a.

Yasuda, Y., Sato, K., and Sugimoto, N.: A Theoretical Study on the Spontaneous Radiation of Inertia-gravity Waves Using the

Renormalization Group Method. Part II: Verification of the Theoretical Equations by Numerical Simulation, J. Atmos. Sci., 72, 984–1009, doi:10.1175/JAS-D-13-0371.1, 2015b.

Yasui, R., Sato, K., and Tsutsumi, M.: Seasonal and interannual variation of mesospheric gravity waves based on MF radar observations over 15 years at Syowa Station in the Antarctic., SOLA, 12, 46–50, doi:10.2151/sola.2016-010, 2016.

Yoshiki, M. and Sato, K.: A statistical study of gravity waves in the polar regions based on operational radiosonde data, J. Geophys. Res., 105, 17995–18011, 2000.

Zhang, F., Koch, S. E., Davis, C. A., and Kaplan, M. L.: Wavelet analysis and the governing dynamics of a large-amplitude mesoscale gravity-wave event along the East Coast of the United States, Q. J. Roy. Meteor. Soc., 127, 2209–2245, 2001.